# Scale- and Variable-Dependent Localization for 3DEnVar Data Assimilation in the Rapid Refresh Forecast System

**Sho YOKOTA[1,2,3], Jacob R. CARLEY[3], Ting LEI[4,3], Shun LIU[3], Daryl T. KLEIST[3], Yongming WANG[5], and Xuguang WANG[5]**

[1]Numerical Prediction Development Center, Japan Meteorological Agency, Tsukuba, Ibaraki, Japan
[2]Meteorological Research Institute, Japan Meteorological Agency, Tsukuba, Ibaraki, Japan
[3]NOAA/NWS/NCEP/Environmental Modeling Center, College Park, Maryland, USA
[4]Lynker, College Park, Maryland, USA
[5]University of Oklahoma, Norman, Oklahoma, USA

Corresponding author: Sho Yokota (syokota@mri-jma.go.jp)

**Key Points:**

- This study implements scale- and variable-dependent localization (SDL and VDL) for data assimilation of the Rapid Refresh Forecast System.
- SDL decreases the imbalance of the analysis field and the bias of temperature and humidity forecasts by the larger localization radius.
- VDL enables simultaneous assimilation of conventional and radar reflectivity data without introducing noisy analysis increments.

# Abstract

This study demonstrates the advantages of scale- and variable-dependent localization (SDL and VDL) on three-dimensional ensemble variational data assimilation of the hourly-updated high-resolution regional forecast system, the Rapid Refresh Forecast System (RRFS). SDL and VDL apply different localization radii for each spatial scale and variable, respectively, by extended control vectors. Single-observation assimilation tests and cycling experiments with RRFS indicated that SDL can enlarge the localization radius without increasing the sampling error caused by the small ensemble size and decreased associated imbalance of the analysis field, which was effective at decreasing the bias of temperature and humidity forecasts. Moreover, simultaneous assimilation of conventional and radar reflectivity data with VDL, where a smaller localization radius was applied only for hydrometeors and vertical wind, improved precipitation forecasts without introducing noisy analysis increments. Statistical verification showed that these impacts contributed to forecast error reduction, especially for low-level temperature and heavy precipitation.

## Plain Language Summary

In atmospheric data assimilation based on ensemble forecasts, the analysis increment is limited to the vicinity of each observation by spatial localization to prevent spurious analysis increments due to sampling error caused by the small ensemble size. Scale- and variable-dependent localization (SDL and VDL) make it possible to set optimal localization radii separately for each spatial scale and variable. Sensitivity experiments in this study with a high-resolution forecast system showed that SDL could decrease the bias of temperature and humidity forecasts and that VDL could improve precipitation forecasts without introducing noisy analysis increments.

# 1. Introduction

To improve short-term high-resolution forecasts of severe weather, it is important to develop high-frequency ensemble-based atmospheric data assimilation (DA) methods (e.g., Dong and Xue 2013; Johnson and Wang 2017). Such methods utilize a high-resolution ensemble to estimate and evolve background error covariance (BEC), providing flow dependent covariances for the data assimilation algorithm. Two of the more common ensemble-based DA methods to assimilate high-resolution observations, such as radar data, are the ensemble Kalman filter (EnKF, Evensen 1994) and the ensemble-variational (EnVar, Hamill and Snyder 2000; Lorenc 2003).

In ensemble-based DA such as with EnKF and EnVar methods, the impact of assimilating observations is generally limited to the local vicinity of each observation utilizing spatial localization (Hamill et al. 2001; Houtekamer and Mitchell 2001). This spatial localization is required to mitigate the sampling error caused by the small ensemble sizes ~$O(10^2)$. However, the small spatial localization limits the spatial extent of synoptic-scale analysis increments and introduces the dynamical imbalance of the analysis (e.g., Greybush et al. 2011).

To account for the disadvantage of small spatial localization, several multiscale localization methods were proposed. Zhang et al. (2009) suggested the successive covariance localization (SCL), which involves running the EnKF algorithm twice; the first pass uses a larger localization radius for so-called large-scale observations (e.g. rawinsondes) and a second pass

uses a shorter localization radius to assimilate dense convective-scale observations, such as those from Doppler radars. Miyoshi and Kondo (2013) suggested another two-step EnKF, which combines two independent EnKF analysis increments in the assimilation of the same observations with different localization radii. For EnVar, Buehner (2012) suggested a similar multiscale localization method, scale-dependent localization (SDL). SDL separates ensemble perturbations into multiple wavebands and different localization radii are simultaneously applied for each perturbation via extended control vectors. Buehner and Shlyaeva (2015) extended this SDL to include cross-scale BECs: this SDL has been tested with several operational global and regional EnVar systems (e.g., Caron and Buehner 2018, 2022; Caron et al. 2019; Huang et al. 2021). Although the simultaneous multiscale localization approach such as SDL is generally not applied in the EnKF with observation-space localization, it is also possible in an EnKF framework with model-space localization such as the multiscale local gain form ensemble transform Kalman filter (Wang et al. 2021).

Although the multiscale localization, such as SDL, attempts to mitigate sampling error without eliminating large-scale analysis increments by setting localization radii separately for synoptic- and convective-scales, the optimal localization radius also may depend on the control variables. In particular, the optimal localization radii of hydrometeors are smaller than other atmospheric variables, such as horizontal wind, temperature, and humidity (e.g., Michel et al. 2011). Furthermore, a smaller localization radius is generally optimal for variables associated

with dense spatial distributions, such as radar data (Perianez et al. 2014). These previous studies indicate the potential necessity of variable-dependent localization (VDL), which uses different localization radii for several variable groups. This facilitates the small-scale update of hydrometeors and the large-scale update of atmospheric variables simultaneously. Wang and Wang (2023a, hereafter WW23) proposed and implemented SDL and VDL simultaneously in a regional EnVar system including radar DA and showed its advantage in a supercell case. Wang and Wang (2023b) further applied this EnVar system to a CONUS case study of squall lines and demonstrated the benefits of SDL and VDL over the single-scale localization method in extracting information from the assimilated conventional in-situ and radar reflectivity observations.

As shown in WW23, SDL and VDL are beneficial in the regional EnVar framework, especially for radar DA. On the other hand, it has not been clear what kind of forecast indicators are statistically improved by application of SDL and VDL in an operational high-frequency DA system, or how much they are improved. This study implements SDL and VDL in the EnVar algorithm of the Rapid Refresh Forecast System (RRFS, Carley et al. 2023), which is the hourly-updated high-resolution (3 km grid spacing) regional forecast system being developed as the next operational regional forecast system for the National Weather Service. Further, we demonstrate which aspects of the forecast are improved when applying SDL and VDL by examining impacts on near surface sensible weather, upper air forecast scores, and precipitation

via a series of sensitivity experiments. In particular, we focus on the impact of SDL and VDL on decreasing the imbalance of the analysis.

The remainder of this paper is organized as follows. Section 2 explains the formulation of SDL and VDL. Section 3 describes the experimental design of the SDL and VDL sensitivity experiments. Section 4 describes the results of the experiments and discusses the impact of SDL and VDL on the analysis and the forecast in the case of Hurricane Ian in 2022. Section 5 presents the conclusions.

# 2. Formulation

*a. Hybrid 3DEnVar*

This study implements SDL and VDL in the Gridpoint Statistical Interpolation (GSI)-based hybrid three-dimensional EnVar (3DEnVar) system (Wang et al. 2013). In this hybrid 3DEnVar, the analysis increment $\delta\mathbf{x}$ is obtained by minimization of the cost function:

$$J(\delta\mathbf{x}_{st}, \mathbf{a}_1, \dots, \mathbf{a}_K) = \frac{1}{2}\beta_{st}(\delta\mathbf{x}_{st})^T\mathbf{B}_{st}^{-1}(\delta\mathbf{x}_{st}) + \frac{1}{2}\beta_{en}\sum_{k=1}^{K}(\mathbf{a}_k)^T\mathbf{L}^{-1}(\mathbf{a}_k) + \frac{1}{2}(\mathbf{H}\delta\mathbf{x}-\mathbf{d})^T\mathbf{R}^{-1}(\mathbf{H}\delta\mathbf{x}-\mathbf{d}), \quad (1)$$

$$\delta\mathbf{x} = \delta\mathbf{x}_{st} + \sum_{k=1}^{K}\begin{bmatrix}\mathbf{a}_k \circ \mathbf{x}_k^{en(1)} \\ \vdots \\ \mathbf{a}_k \circ \mathbf{x}_k^{en(I)}\end{bmatrix}, \quad (2)$$

where $\delta\mathbf{x}_{st}$ and $\mathbf{a}_k$ ($k = 1, \dots, K$; $K$ is the ensemble size) are $NI$- and $N$-dimension control vectors, respectively ($N$ and $I$ are the number of analysis grid points and the number of variables, respectively), $\mathbf{B}_{st}$ in the first term of the right-hand side of Eq. (1) denotes the static BEC ($NI \times NI$ matrix), $\mathbf{L}$ in the second term denotes the localization ($N \times N$ matrix),

and $\mathbf{R}$, $\mathbf{H}$, and $\mathbf{d}$ in the third term denote the observation error covariance ($M \times M$ matrix), the linearized observation operator ($M \times NI$ matrix), and the $M$-dimension observation innovation vector, respectively ($M$ is the number of assimilated observations). $\beta_{st}$ and $\beta_{en}$ ($1/\beta_{st} + 1/\beta_{en} = 1$) are the weights of the static and ensemble BECs, respectively. $\mathbf{x}_k^{en(i)}$ in Eq. (2) is the $N$-dimension $k$-th ensemble perturbation vector ($k$-th ensemble member subtracted by ensemble mean and normalized by $\sqrt{K-1}$) of the $i$-th kind of variable ($i = 1, \ldots, I$) and "$\circ$" denotes the Schur product.

*b. Scale- and variable-dependent localization*

Earlier studies (Buehner and Shlyaeva 2015; Caron and Buehner 2018; Huang et al. 2021) have implemented and explored SDL in the EnVar context. WW23 further proposed and implemented both SDL and VDL within the GSI-based EnVar system. This subsection explains how to implement SDL and VDL, mainly mirroring the notations of WW23. The scale separation method for SDL realized by the recursive filter (Purser et al. 2003) is also shown here.

In the formulation for SDL and VDL, the control vector $\mathbf{a}_k$ in Eq. (1) is extended to $NSV$-dimension ($S$ and $V$ denote the total numbers of scales in SDL and variable groups in VDL, respectively) as

$$\mathbf{a}_k = \begin{bmatrix} \begin{pmatrix} \mathbf{a}_{k,1,1} \\ \vdots \\ \mathbf{a}_{k,1,V} \end{pmatrix} \\ \vdots \\ \begin{pmatrix} \mathbf{a}_{k,S,1} \\ \vdots \\ \mathbf{a}_{k,S,V} \end{pmatrix} \end{bmatrix}, \tag{3}$$

and the analysis increment is written as

$$\delta\mathbf{x} = \delta\mathbf{x}_{st} + \sum_{k=1}^{K}\sum_{s=1}^{S} \begin{bmatrix} \mathbf{a}_{k,s,v(1)} \circ \mathbf{x}_{k,s}^{en(1)} \\ \vdots \\ \mathbf{a}_{k,s,v(I)} \circ \mathbf{x}_{k,s}^{en(I)} \end{bmatrix}, \tag{4}$$

where $v(i)$ $[1 \le v(i) \le V]$ denotes the variable group number including the $i$-th variable. Compared to Eq. (2), $\delta\mathbf{x}$ is created by the summation of each scale analysis increment and $\mathbf{a}_{k,s,v(i)}$ is multiplied to the ensemble perturbations $\mathbf{x}_{k,s}^{en(i)}$ separately for each scale $s$ and variable group $v(i)$.

In this formulation, the localization $\mathbf{L}$ is also extended to $NSV \times NSV$ matrix as

$$\mathbf{L} = \begin{bmatrix} c_{1,1}^{s}\begin{pmatrix} c_{1,1}^{v}\mathbf{L}_{1,1}^{1/2}\mathbf{L}_{1,1}^{T/2} & \cdots & c_{1,V}^{v}\mathbf{L}_{1,1}^{1/2}\mathbf{L}_{1,V}^{T/2} \\ \vdots & \ddots & \vdots \\ c_{V,1}^{v}\mathbf{L}_{1,V}^{1/2}\mathbf{L}_{1,1}^{T/2} & \cdots & c_{V,V}^{v}\mathbf{L}_{1,V}^{1/2}\mathbf{L}_{1,V}^{T/2} \end{pmatrix} & \cdots & c_{1,S}^{s}\begin{pmatrix} c_{1,1}^{v}\mathbf{L}_{1,1}^{1/2}\mathbf{L}_{S,1}^{T/2} & \cdots & c_{1,V}^{v}\mathbf{L}_{1,1}^{1/2}\mathbf{L}_{S,V}^{T/2} \\ \vdots & \ddots & \vdots \\ c_{V,1}^{v}\mathbf{L}_{1,V}^{1/2}\mathbf{L}_{S,1}^{T/2} & \cdots & c_{V,V}^{v}\mathbf{L}_{1,V}^{1/2}\mathbf{L}_{S,V}^{T/2} \end{pmatrix} \\ \vdots & \ddots & \vdots \\ c_{S,1}^{s}\begin{pmatrix} c_{1,1}^{v}\mathbf{L}_{S,1}^{1/2}\mathbf{L}_{1,1}^{T/2} & \cdots & c_{1,V}^{v}\mathbf{L}_{S,1}^{1/2}\mathbf{L}_{1,V}^{T/2} \\ \vdots & \ddots & \vdots \\ c_{V,1}^{v}\mathbf{L}_{S,V}^{1/2}\mathbf{L}_{1,1}^{T/2} & \cdots & c_{V,V}^{v}\mathbf{L}_{S,V}^{1/2}\mathbf{L}_{1,V}^{T/2} \end{pmatrix} & \cdots & c_{S,S}^{s}\begin{pmatrix} c_{1,1}^{v}\mathbf{L}_{S,1}^{1/2}\mathbf{L}_{S,1}^{T/2} & \cdots & c_{1,V}^{v}\mathbf{L}_{S,1}^{1/2}\mathbf{L}_{S,V}^{T/2} \\ \vdots & \ddots & \vdots \\ c_{V,1}^{v}\mathbf{L}_{S,V}^{1/2}\mathbf{L}_{S,1}^{T/2} & \cdots & c_{V,V}^{v}\mathbf{L}_{S,V}^{1/2}\mathbf{L}_{S,V}^{T/2} \end{pmatrix} \end{bmatrix}, \tag{5}$$

where $\mathbf{L}_{s,v}^{1/2}$ denotes square root of the localization matrix $\mathbf{L}_{s,v}$ ($N \times N$ matrix) and is realized by the recursive filter for the $s$-th scale in SDL and for the $v$-th variable group in VDL. $c_{s_1,s_2}^{s}$ $(s_1, s_2 = 1, \ldots, S)$ and $c_{v_1,v_2}^{v}$ $(v_1, v_2 = 1, \ldots, V)$ are factors multiplying cross-scale and cross-variable correlations, respectively. If $c_{s_1,s_2}^{s} = 1$ ("Cross" in Huang et al. 2021) and $c_{v_1,v_2}^{v} = 1$ in all scales and variables, $\mathbf{L}$ is represented simply as

$$\mathsf{L} = \begin{bmatrix} \begin{pmatrix} \mathsf{L}_{1,1}^{1/2} \\ \vdots \\ \mathsf{L}_{1,V}^{1/2} \end{pmatrix} \\ \vdots \\ \begin{pmatrix} \mathsf{L}_{S,1}^{1/2} \\ \vdots \\ \mathsf{L}_{S,V}^{1/2} \end{pmatrix} \end{bmatrix} \left[ \left( \mathsf{L}_{1,1}^{T/2} \quad \cdots \quad \mathsf{L}_{1,V}^{T/2} \right) \quad \cdots \quad \left( \mathsf{L}_{S,1}^{T/2} \quad \cdots \quad \mathsf{L}_{S,V}^{T/2} \right) \right]. \tag{6}$$

On contrary, if $c_{s_1,s_2}^{s} = \delta_{s_1 s_2}$ ("NoCross" in Huang et al. 2021) and $c_{v_1,v_2}^{v} = \delta_{v_1 v_2}$, all cross-scale and cross-variable correlations are ignored as

$$\mathsf{L} = \begin{bmatrix} \begin{pmatrix} \mathsf{L}_{1,1}^{1/2} & & \mathbf{0} \\ & \ddots & \\ \mathbf{0} & & \mathsf{L}_{1,V}^{1/2} \end{pmatrix} & & \mathbf{0} \\ & \ddots & \\ \mathbf{0} & & \begin{pmatrix} \mathsf{L}_{S,1}^{1/2} & & \mathbf{0} \\ & \ddots & \\ \mathbf{0} & & \mathsf{L}_{S,V}^{1/2} \end{pmatrix} \end{bmatrix} \begin{bmatrix} \begin{pmatrix} \mathsf{L}_{1,1}^{T/2} & & \mathbf{0} \\ & \ddots & \\ \mathbf{0} & & \mathsf{L}_{1,V}^{T/2} \end{pmatrix} & & \mathbf{0} \\ & \ddots & \\ \mathbf{0} & & \begin{pmatrix} \mathsf{L}_{S,1}^{T/2} & & \mathbf{0} \\ & \ddots & \\ \mathbf{0} & & \mathsf{L}_{S,V}^{T/2} \end{pmatrix} \end{bmatrix}. \tag{7}$$

In this study, the scale separation to obtain $\mathbf{x}_{k,s}^{en(i)}$ from the original ensemble perturbation $\mathbf{x}_{k}^{en(i)}$ is achieved as

$$\mathbf{x}_{k,s}^{en(i)} = \begin{cases} \mathsf{F}_{s,v(i)} \mathbf{x}_{k}^{en(i)} & (s = 1) \\ \mathsf{F}_{s,v(i)} \left[ \mathbf{x}_{k}^{en(i)} - \mathbf{x}_{k,s-1}^{en(i)} \right] & (1 < s < S) \\ \mathbf{x}_{k}^{en(i)} - \mathbf{x}_{k,S-1}^{en(i)} & (s = S), \end{cases} \tag{8}$$

where $\mathsf{F}_{s,v}$ is the low-pass filter realized by the recursive filter for the $s$-th scale in SDL and the $v$-th variable group in VDL. The recursive filter in calculating $\mathsf{F}_{s,v}$ should be normalized to make the spatially-integrated value one while that in calculating $\mathsf{L}_{s,v}$ is normalized to make the peak value one. The resulting power spectra of $\mathbf{x}_{k,s}^{en(i)}$ are quasi-Gaussian in the wave space (see Appendix A). The scale separation based on Eq. (8) obtains each scale in order from the largest scale with the recursive filter, which is not strictly the same as the approach used in WW23 applying the diffusion operator in order from the smallest scale. However, the resulting power spectra was almost the same (not shown) and the computational expense of Eq. (8) is

less than that of WW23 because the computationally-efficient recursive filter is used instead of the diffusion operator.

# 3. Experimental design

In this study, we implemented SDL and VDL in hybrid 3DEnVar of a prototype RRFS (Carley et al. 2023). First, we conducted the control experiment of single scale localization (SSL) without radar reflectivity DA and compared it to the experiment with SDL. After that, we additionally assimilated radar reflectivity in the experiment with VDL and compared it to the control experiment. As a reference, the experiment with the early operational multiscale approach, which runs 3DEnVar twice with different localization radii for large- and convective-scale observations (SCL), was conducted. We also include comparisons with experiments using both SDL and SCL as well as with both SDL and VDL. These experiments will be explained in more detail later in this section.

The RRFS is the high-resolution forecast system based on the limited area model capability for the non-hydrostatic finite-volume cubed-sphere dynamical core (FV3LAM, Lin 2004; Putman and Lin 2007; Black et al. 2021), which is being developed as the next-generation operational regional forecast systems in National Centers for Environmental Prediction (NCEP) and may replace several existing regional systems [e.g., the North American Mesoscale (NAM; Janjic 2003; Janjic and Gall 2012) 3-km nests and High-Resolution Ensemble Forecast system

(HREF; Roberts et al. 2019, 2020)]. The horizontal grid interval is 3 km. The number of vertical layers is 65 and the lowest level thickness and the top of the model are 8 m and 2 hPa, respectively. Although the operational RRFS will cover a North American domain, this study applies it only for the CONUS (contiguous United States) domain and the number of grid cells is 1820 x 1092 horizontally. Physics schemes used in the FV3LAM for this study are listed in Table 1.

The schematics of the procedure of the experiments for this study are shown in Fig. 1. Here, hourly analysis-forecast cycles with GSI-based 3DEnVar and FV3LAM (initiated at 03 and 15 UTC) and 36-hour forecasts (from the 3DEnVar analysis at 12 and 00 UTC) were repeated every 12 hours. The BEC in 3DEnVar was purely ensemble-based and created by 1-hour FV3LAM ensemble forecasts from the 30-member serial ensemble square root filter (EnSRF; Whitaker and Hamill 2002). The EnSRF analysis mean was replaced with the 3DEnVar analysis (recentering in Fig. 1) and the ensemble spread was inflated by the relaxation-to-prior spread method (RTPS; Whitaker and Hamill, 2012) with the factor of 0.85. Only for the analyses at 03 and 15 UTC, the BEC was created using a 9-hour global ensemble forecast subset from the 80-member local gain form ensemble transform Kalman filter (LGETKF; Hunt et al. 2007; Lei et al. 2018) run as a part of the Global DA System (GDAS) operated by NCEP. The initial conditions (ICs), namely the first guesses of the 3DEnVar and the initial states of 30-member ensemble forecasts, were created by 3-hour deterministic forecasts in the Global Forecast

System (GFS) in NCEP and by 9-hour global ensemble forecasts in GDAS (30 of 80 members), respectively, under constraints of operational availability. The deterministic forecasts of GFS were also used for the lateral boundary conditions (LBCs) of all FV3LAM forecasts in the experiments for this study, meaning also that lateral boundary perturbations were not introduced for the ensemble.

To verify the impacts of SDL for synoptic-scale analysis and VDL for radar reflectivity DA, five sensitivity experiments were conducted in this study along with the control simulation. The control experiment (hereafter CNTL) assimilated a similar set of observations associated with the Rapid Refresh (RAP; Benjamin et al. 2004, 2016) and High Resolution Rapid Refresh (HRRR; Dowell et al. 2022), which includes observations from METAR, rawinsondes, aircraft, and radial winds of Weather Surveillance Radar-1988 Doppler (WSR-88D; Crum and Alberty 1993, Liu et al. 2016), in both 3DEnVar and EnSRF. Satellite radiance data was not assimilated. The localization radii are prescribed somewhat differently between their respective implementations in EnSRF and 3DEnVar algorithms. The former defines the radii as the cutoff scale of the Gaspari-Cohn localization function (Gaspari and Cohn 1999) while the latter uses the Gaussian localization function ($e^{-20/3}$-folding scale). Therefore, the localization radii were set to 300 km horizontally and 1.1 scale heights vertically, while the corresponding $e^{-1/2}$-folding scale in 3DEnVar was 82.158 km horizontally and 0.30125 scale heights vertically. After 3DEnVar only, the lowest-level and soil temperature and specific humidity were adjusted

by land-snow DA with satellite-based soil temperature and specific humidity data (Benjamin et al. 2022), and hydrometeors were adjusted by non-variational cloud-hydrometeor assimilation with radar reflectivity and lightning data (Benjamin et al. 2021).

The difference in the settings of the sensitivity experiments are summarized in Table 2. Neither SDL nor VDL was applied in CNTL ($L = 1$ and $J = 1$). In the experiment with SDL (hereafter EXPSDL), only the horizontal localization radii in 3DEnVar were different from CNTL and set to 1200 and 300 km for larger and smaller-scale ensemble perturbations with 2-scale SDL ($L = 2$ and $J = 1$) including cross-scale covariance ($c^s_{1,1} = c^s_{1,2} = c^s_{2,1} = c^s_{2,2} = 1$). These 2 scales were separated by the horizontal recursive filter with 300-km $e^{-20/3}$-folding scale as shown in Fig. 2. The other four experiments directly assimilated radar reflectivity with the method of Wang and Wang (2017) only in 3DEnVar, where the non-variational cloud-hydrometeor assimilation (Benjamin et al. 2021) done in CNTL and EXPSDL was limited to just clearing out rain, snow, and graupel without radar reflectivity observations. Here, only 10 dBZ and larger reflectivity data interpolated to the analysis grids were assimilated directly, and 5 dBZ and less reflectivity data, thinned at every other horizontal and vertical grid point, were also assimilated as 0 dBZ observations. The observation error standard deviation was set to 5 dBZ. In EXP2DA, radar reflectivity was assimilated in the second pass of 3DEnVar with the smaller horizontal localization radius (15-km $e^{-20/3}$-folding scale) just after the other observations were assimilated in the first 3DEnVar pass (SCL in Zhang et al. 2009). In

EXPVDL, on the other hand, radar reflectivity was assimilated simultaneously with the other observations in a single 3DEnVar instance using VDL ($L = 1$ and $J = 2$): the horizontal localization radii were set to 300 km for the conventional analysis variables (i.e., horizontal wind, temperature, specific humidity, and surface pressure), and 15 km for the other analysis variables added for the radar reflectivity DA (i.e., vertical wind, reflectivity, and mixing ratios of cloud water, cloud ice, rain, snow, and graupel). The cross-variable covariance between these two variable groups was decreased by multiplying the factor 0.05 (=15/300) to prevent too large impacts of radar reflectivity DA ($c^v_{1,1} = c^v_{2,2} = 1$ and $c^v_{1,2} = c^v_{2,1} = 0.05$, see Appendix B). EXPSDL2DA was the same as EXP2DA except applying SDL ($L = 2$ and $J = 1$) only for the first 3DEnVar like EXPSDL. EXPSDLVDL was the same as EXPVDL except applying SDL for atmospheric variables in addition to VDL ($L = 2$ and $J = 2$). In all experiments, the other settings including the vertical localization radius were the same as CNTL. In all applications of the EnSRF, radar reflectivity was not assimilated and neither SDL nor VDL was used.

We set the experimental period of the analysis-forecast cycles from 03 UTC, May 11 to 12 UTC, May 19, 2021 and from 15 UTC, September 29 to 00 UTC, September 30, 2022. These periods were chosen to examine the impact of SDL and VDL in cases of severe local storms (the former period) and a tropical cyclone (the latter). In May 2021, 287 tornadoes, the largest in 2021, were reported in the U.S. For the May 11–19 period, most tornadoes were generated in the south-central U.S. The strongest tornado in this period was generated in Texas at 0011

UTC on May 18 and ranked as EF2 (NCEI 2023). In September 2022, Hurricane Ian produced catastrophic storm surge, winds, and floods. Ian reached its peak intensity of 72.0 m $s^{-1}$ (a category 5 hurricane) at 1200 UTC, 28 September, and made landfall in southwestern Florida with winds of 66.9 m $s^{-1}$ at 1905 UTC, September 28, and in South Carolina with winds of 36.0 m $s^{-1}$ at 1805 UTC, September 30 (Bucci et al. 2023).

Table 1. List of physics schemes used in FV3-LAM.

| Physics schemes | Specification |
|---|---|
| Cloud microphysics | Thompson-Eidhammer Aerosol Aware Microphysics (Thompson and Eidhammer 2014) |
| Planetary boundary layer | Mellor-Yamada-Nakanishi-Niino Eddy Diffusivity/Mass Flux (MYNN-EDMF; Nakanishi and Niino 2009; Olson et al. 2019; Angevine et al. 2020) |
| Surface layer | Mellor-Yamada-Nakanishi-Niino surface layer (Olson et al. 2021) |
| Gravity wave | Small Scale Gravity Wave Drag (SSGWD; Tsiringakis et al. 2017) and Turbulent Orographic Form Drag (TOFD; Beljaars et al. 2004) |
| Land | Rapid Update Cycle Land Surface Model (RUC LSM; Smirnova et al. 1997, 2000, 2016) |
| Long and short-wave radiation | Rapid Radiative Transfer Model for Global Circulation Models (RRTMG; Mlawer 1997; Iacono et al. 2008) |

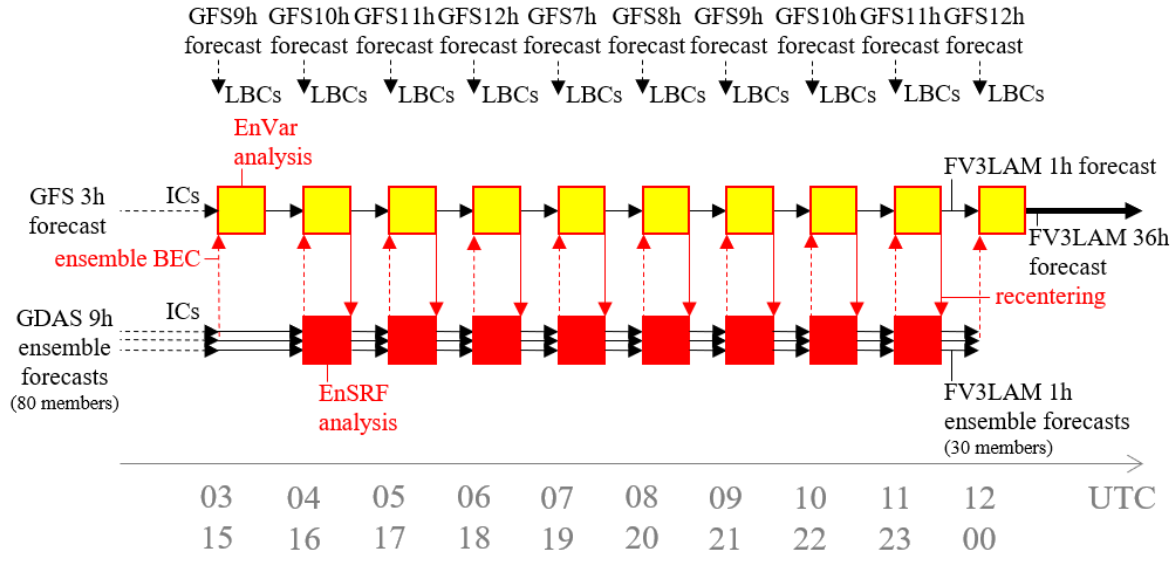


Fig. 1. Schematics of analysis-forecast cycling experiments.

Table 2. List of settings of EnVar in sensitivity experiments.

| Name | Radar reflectivity DA | Horizontal localization radius ($e^{-20/3}$ scale) |
|---|---|---|
| CNTL | Not assimilated | 300 km |
| EXPSDL | Not assimilated | 1200 km (large-scale)<br>300 km (small-scale) |
| EXP2DA | Assimilated separately after conventional DA | 300 km (conventional DA)<br>15 km (radar reflectivity DA) |
| EXPSDL2DA | Assimilated separately after conventional DA | 1200 km (large-scale in conventional DA)<br>300 km (small-scale in conventional DA)<br>15 km (radar reflectivity DA) |
| EXPVDL | Assimilated simultaneously with conventional DA | 300 km (atmosphere)<br>15 km (hydrometeors) |
| EXPSDLVDL | Assimilated simultaneously with conventional DA | 1200 km (large-scale atmosphere)<br>300 km (small-scale atmosphere)<br>15 km (large-scale hydrometeors)<br>15 km (small-scale hydrometeors) |

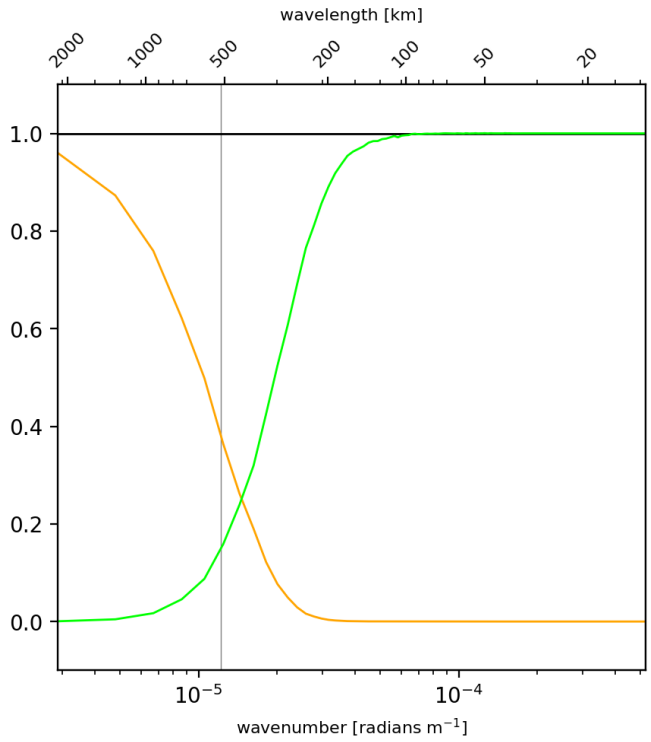


Fig. 2. The power spectrum density ratio of ensemble perturbations in SDL (black: original perturbation; orange: filtered perturbation by recursive filter; green: difference between original and filtered perturbations). Gray solid line indicates characteristic wavelength in scale separation (recursive filter $e^{-1/2}$-folding scale).

# 4. Results and discussion

*a. Single observation experiments*

In this subsection, we examine the impact of SDL and VDL first via a single observation experiment with pseudo surface pressure observation using the settings of CNTL, EXPSDL, and EXPVDL. We also include two additional experiments that are configured in the same manner as CNTL except use a single-scale horizontal localization radii ($e^{-20/3}$ scale) of 1200 km and 15 km (hereafter EXPSSL1200 and EXPSSL15, respectively). The horizontal localization function in each experiment is shown in Fig. 3. Each single observation experiment uses the same first guess field. The pseudo surface pressure observation having a first guess departure of –10 hPa and an observation error standard deviation of 1 hPa was assimilated in the northern region of Hurricane Ian at 80W and 31N at 16 UTC on September 29, 2022.

Figure 4 shows the analysis increments of the lowest-level temperature and sea level pressure (SLP) analysis in CNTL, EXPSSL1200, and EXPSDL. In CNTL, the analysis increments were limited within the northern part of the hurricane and the resulting surface pressure analysis was inconsistent with the expected axisymmetric hurricane structure (Fig. 4a). In EXPSSL1200, such unrealistic structure was not seen, and the hurricane was reasonably intensified because of the larger localization radius (Fig. 4b). However, the analysis increment was noisy north of the hurricane into South Carolina, likely due to sampling error. In EXPSDL (Fig. 4c), which includes both localization radii of CNTL and EXPSSL1200, the analysis

297 increments cover approximately the same area as EXPSSL1200 but are smoother overall.
298 Further, the analysis increment near the observation location remains similar to that noted in
299 the CNTL. The increments in the EXPSDL single observation experiment suggest that a large-
300 scale impact can be achieved in a way that reduces apparent sampling error.

301 The analysis increments of radar reflectivity at the lowest model level and SLP analysis for
302 CNTL, EXPSSL15, and EXPVDL are also shown in Fig. 5. In CNTL, the horizontal scale of
303 the analysis increment for radar reflectivity was as large as that for temperature (Figs. 4a and
304 5a) based on the localization function shown in the solid gray line in Fig. 3b. In EXPSSL15, on
305 the other hand, the smaller localization radius (dashed gray line in Fig. 3b) severely limits the
306 spatial extent of the analysis increment (Fig. 5b). Such small-scale analysis increments can
307 cause large dynamical imbalance of atmospheric variables. In EXPVDL with both localization
308 radii of CNTL (for horizontal wind, temperature, specific humidity, and surface pressure) and
309 EXPSSL15 (for vertical wind, reflectivity, and hydrometeors), the analysis of atmospheric
310 variables was identical to that in CNTL (compare SLP analyses in Figs. 5a and c). However,
311 the analysis increment of radar reflectivity in EXPVDL was smaller than that in CNTL and its
312 horizontal scale was between those in CNTL and EXPSSL15 (color in Fig. 5c) because the peak
313 value and the $e^{-20/3}$-folding scale of the localization function for cross-variable covariances
314 were approximately 0.005 and 212 km, respectively (see magenta line in Fig. 3b and Appendix
315 B).

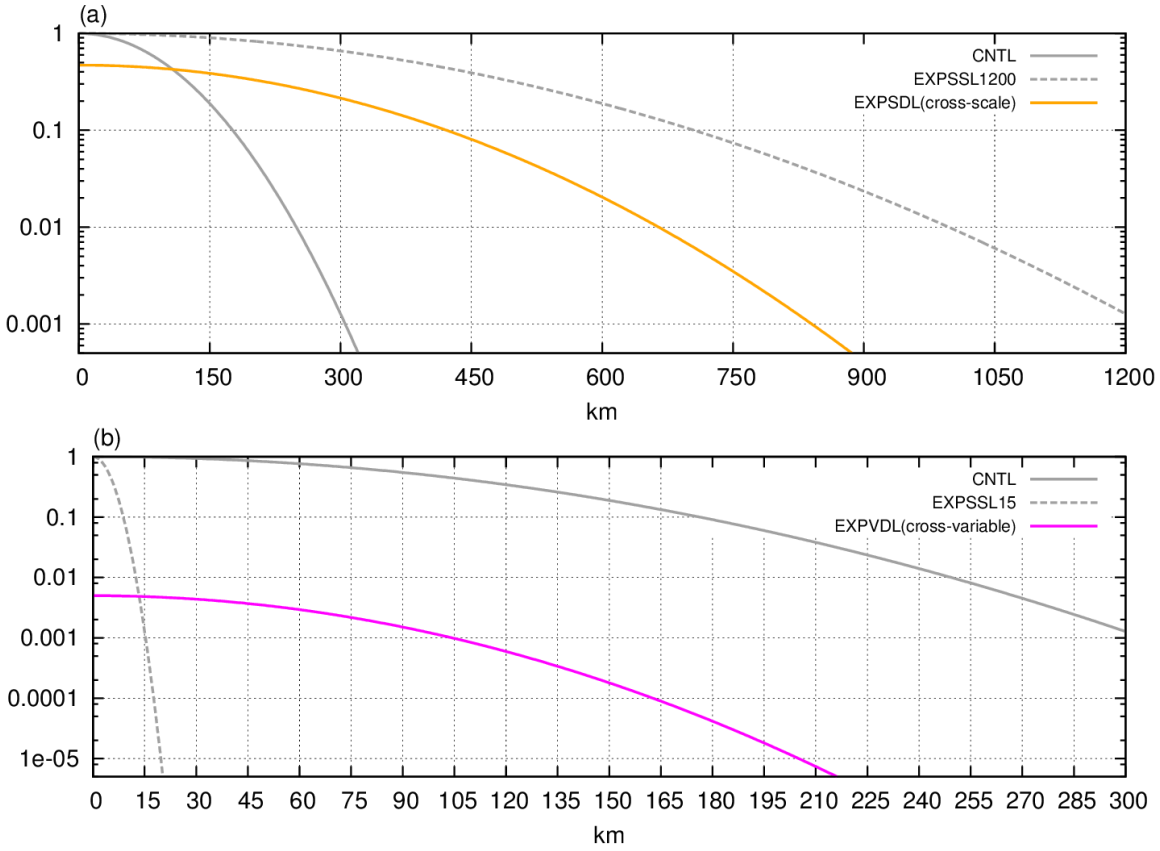


316

317 Fig. 3. Horizontal localization functions [a: CNTL (solid gray), EXPSSL1200 (dashed gray),
318 and EXPSDL for the cross-scale covariance (orange); b: CNTL (solid gray), EXPSSL15
319 (dashed gray), and EXPVDL for the cross-variable covariance (magenta)]. Horizontal axis is
320 the horizontal distance from the analysis point.

321

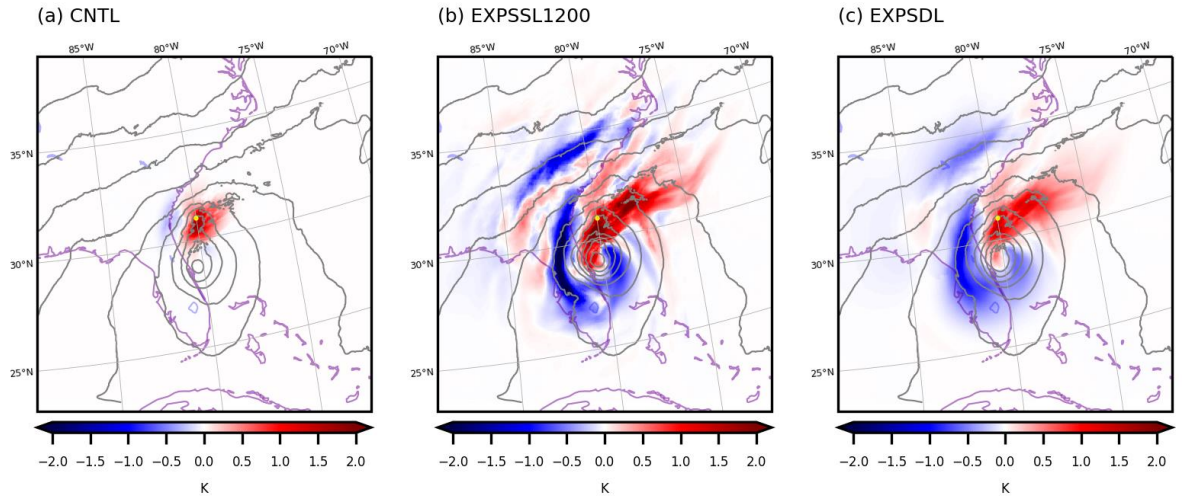


Fig. 4. Analysis increment of lowest-level temperature (color, K) and SLP analysis (gray contours, every 4 hPa) at 16 UTC on September 29, 2022 in the single surface pressure DA experiments (a: CNTL; b: EXPSSL1200; c: EXPSDL). Yellow dot is the position of the assimilated observation.

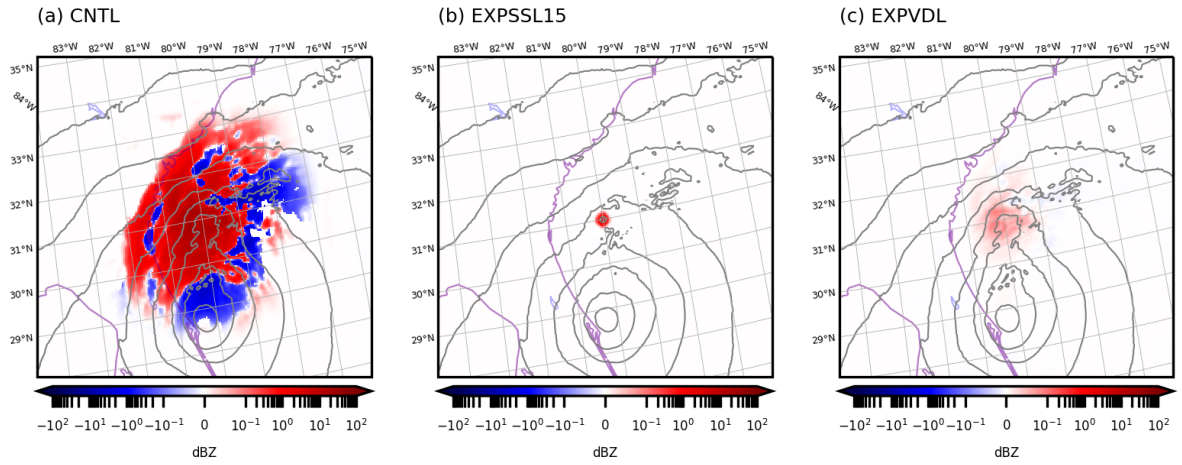


Fig. 5. Analysis increment of lowest-level radar reflectivity (color, dBZ) and SLP analysis (gray contours, every 4 hPa) at 16 UTC on September 29, 2022 in the single surface pressure DA experiments (a: CNTL; b: EXPSSL15; c: EXPVDL).

*b. Statistical verification in cycling experiments*

In this subsection, the impact of SDL and VDL is statistically verified in cycling experiments for May 11–19, 2021. For the verification of atmospheric variables, SDL had more impact than VDL as a whole. The relative impact of radar reflectivity DA to CNTL was almost the same between in two-step EnVar with SCL (EXP2DA and EXPSDL2DA) and in simultaneous EnVar with VDL (EXPVDL and EXPSDLVDL).

Figure 6 shows the first guess departure of assimilated in-situ temperature, relative humidity, and horizontal wind observations. Compared to CNTL, the RMSE was significantly (confidence level $\geq 95\%$) smaller for temperature (Fig. 6a) and near-surface (> 950hPa) relative humidity (Fig. 6b) in the experiments with SDL (EXPSDL, EXPSDL2DA, and EXPSDLVDL). These RMSE reductions were associated with SDL making the horizontally averaged temperature warmer (Fig. 6d) and relative humidity dryer (Fig. 6e), respectively, in the corresponding vertical layers. The RMSE for low-level wind and its strong bias also tended to be smaller in the experiments with SDL (Figs. 6c and f)

The impact of SDL shown above was also seen in the 12-hour upper-air forecast verified against radiosonde data for May 11–19, 2021 (Fig. 7): the cold bias of low-level (> 650hPa) temperature and the moist bias of low-level (> 850 hPa) relative humidity were clearly decreased by SDL. These bias reductions were also clear in the surface verification. Both for temperature (Fig. 8a) and for dew point temperature (Fig. 8b), the cold and moist biases were

352 decreased until the end of the forecast (36 hours). The cause of these bias reductions is discussed
353 in the next section. As for the near surface wind, the impact was neutral (not shown).

354 The radar reflectivity DA slightly increased and decreased the cold bias of low-level and
355 mid-level temperature, respectively (see the differences between the experiments with
356 (EXP2DA, EXPSDL2DA, EXPVDL, and EXPSDLVDL) and without (CNTL and EXPSDL)
357 radar reflectivity DA in Fig. 6d), and their associated RMSEs (Fig. 6a); this impact was
358 associated with increasing near-surface evaporation cooling and midlevel condensation heating.
359 In fact, near-surface and midlevel first guesses of temperature were clearly lower and higher,
360 respectively, in the precipitation region in EXP2DA and EXPVDL than those in CNTL (Fig. 9).
361 Please note that the impact of the radar reflectivity DA was smaller and only seen in the shorter-
362 range forecast than that of SDL (Figs. 6–8) since it was limited to the precipitation region.

363 As for radar reflectivity forecasts, the impacts of both SDL and VDL were clear. Figure 10
364 is the performance diagram (Roebber 2009) of 3-hour and 12-hour composite reflectivity
365 forecasts, which shows success ratio (SR) and probability of detection (POD) verified against
366 the Multi-Radar Multi-Sensor (MRMS, Smith et al. 2016) as horizontal and vertical axes,
367 respectively. In this diagram, points in the upper right indicate the higher critical success index
368 (CSI). Points in the upper left and in the lower right indicate the higher and lower bias,
369 respectively, of the reflectivity forecast. It shows that radar reflectivity DA made both CSI and
370 positive bias larger especially in the short-term forecasts of low reflectivity. This impact was

larger in EXP2DA than in EXPVDL (Fig. 10a) and also seen in 12-hour forecasts except for the high reflectivity (Fig. 10b). This positive bias of reflectivity forecasts was decreased by both SDL and VDL. This SDL-induced bias reduction was larger than its increase by radar reflectivity DA in 12-hour forecasts (Fig. 10b), and retained until the end of (36-hour) forecasts (not shown). Although SDL did not necessarily improve CSI in the 3-hour forecasts (Fig. 10a), it was clearly improved by SDL especially in 12-hour forecasts for high reflectivity (Fig. 10b).

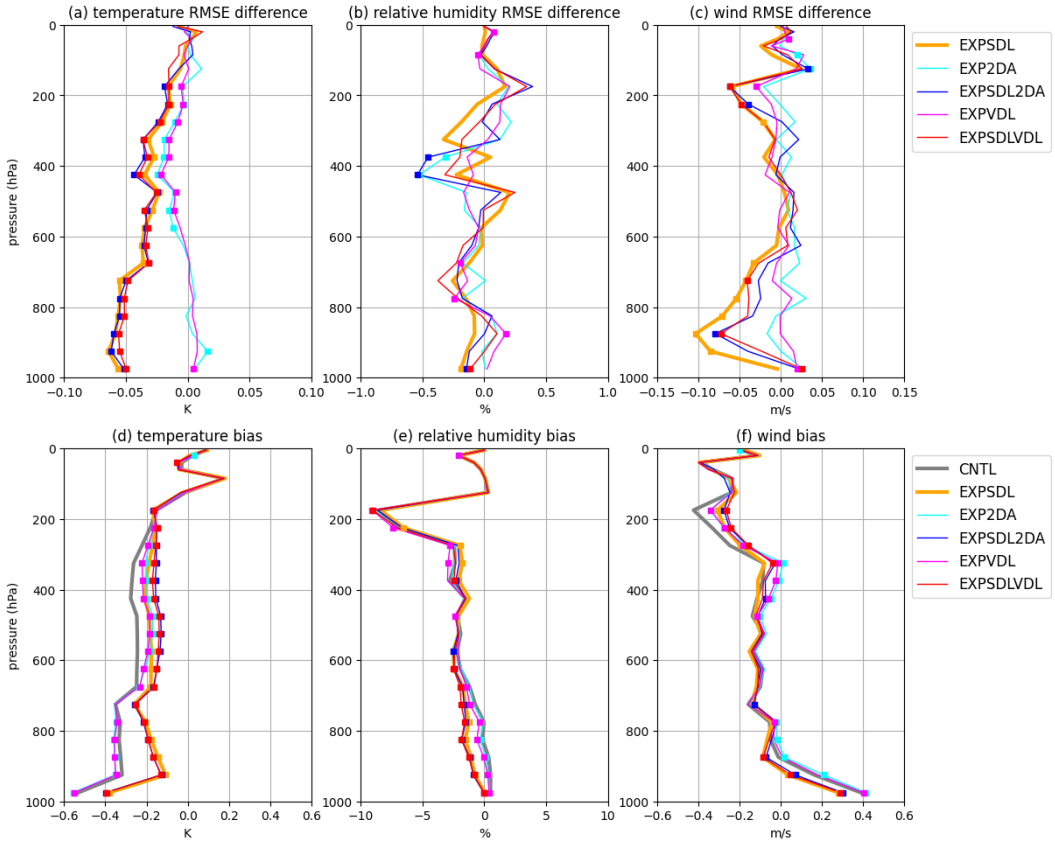


Fig. 6. Vertical profiles of first guess departure (a–c) standard deviations (difference from CNTL) and (d–f) biases verified against assimilated in-situ observations [a and d: temperature (K); b and e: relative humidity (%); c and f: horizontal wind (m $s^{-1}$)] in each cycling experiment for May 11–19, 2021 (gray: CNTL; orange: EXPSDL; cyan: EXP2DA; blue: EXPSDL2DA; magenta: EXPVDL; red: EXPSDLVDL). Square marks indicate significantly different from CNTL (confidence level ≥ 95%).

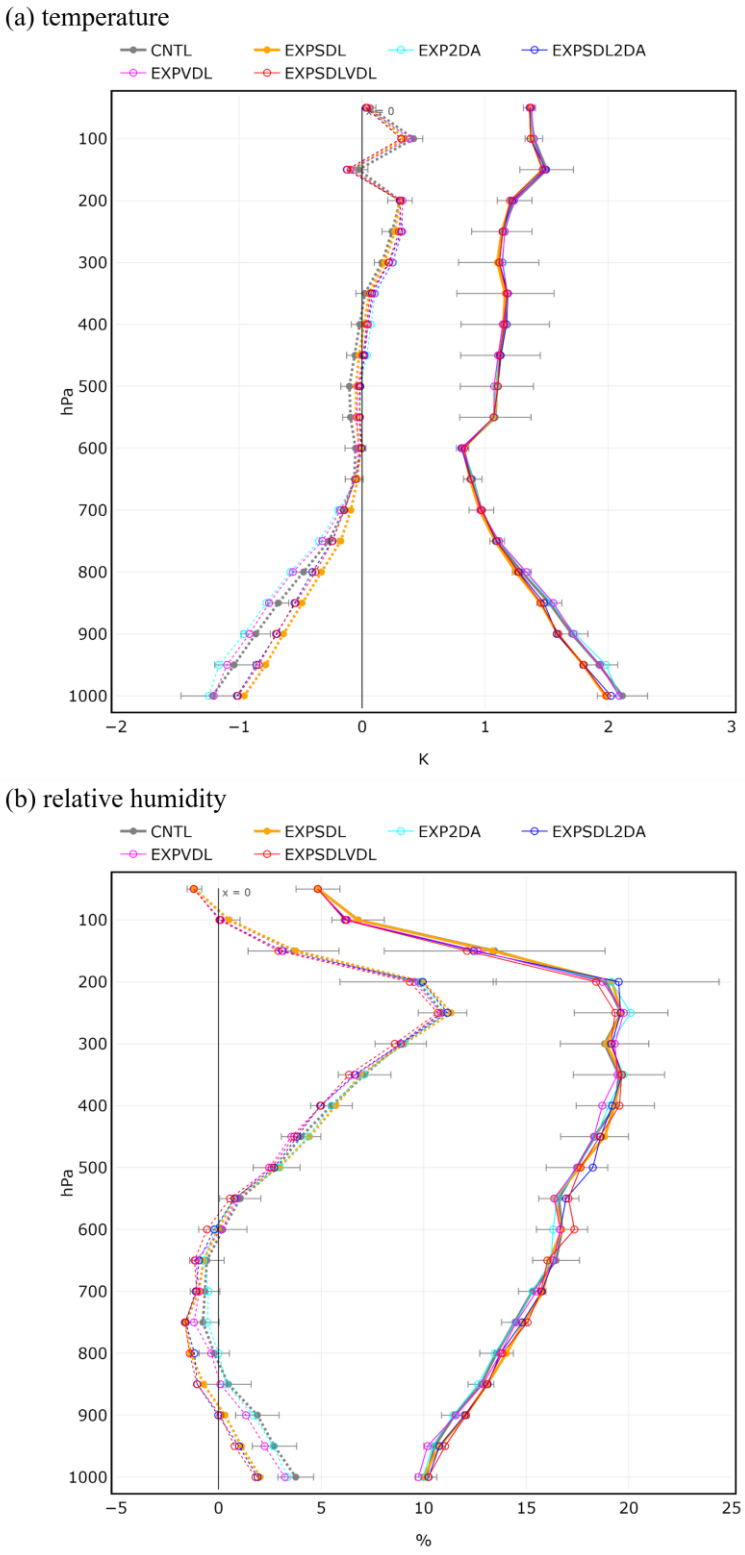


Fig. 7. Vertical profiles of 12-hour forecast RMSE (solid lines) and bias (dotted lines) verified against radiosonde (a) temperature (K) and (b) relative humidity (%) observations in each cycling experiment for May 11–19, 2021 (gray: CNTL; orange: EXPSDL; cyan: EXP2DA; blue: EXPSDL2DA; magenta: EXPVDL; red: EXPSDLVDL). The relative humidity forecast was computed with observed temperature. The error bars show 95% confidence in CNTL.

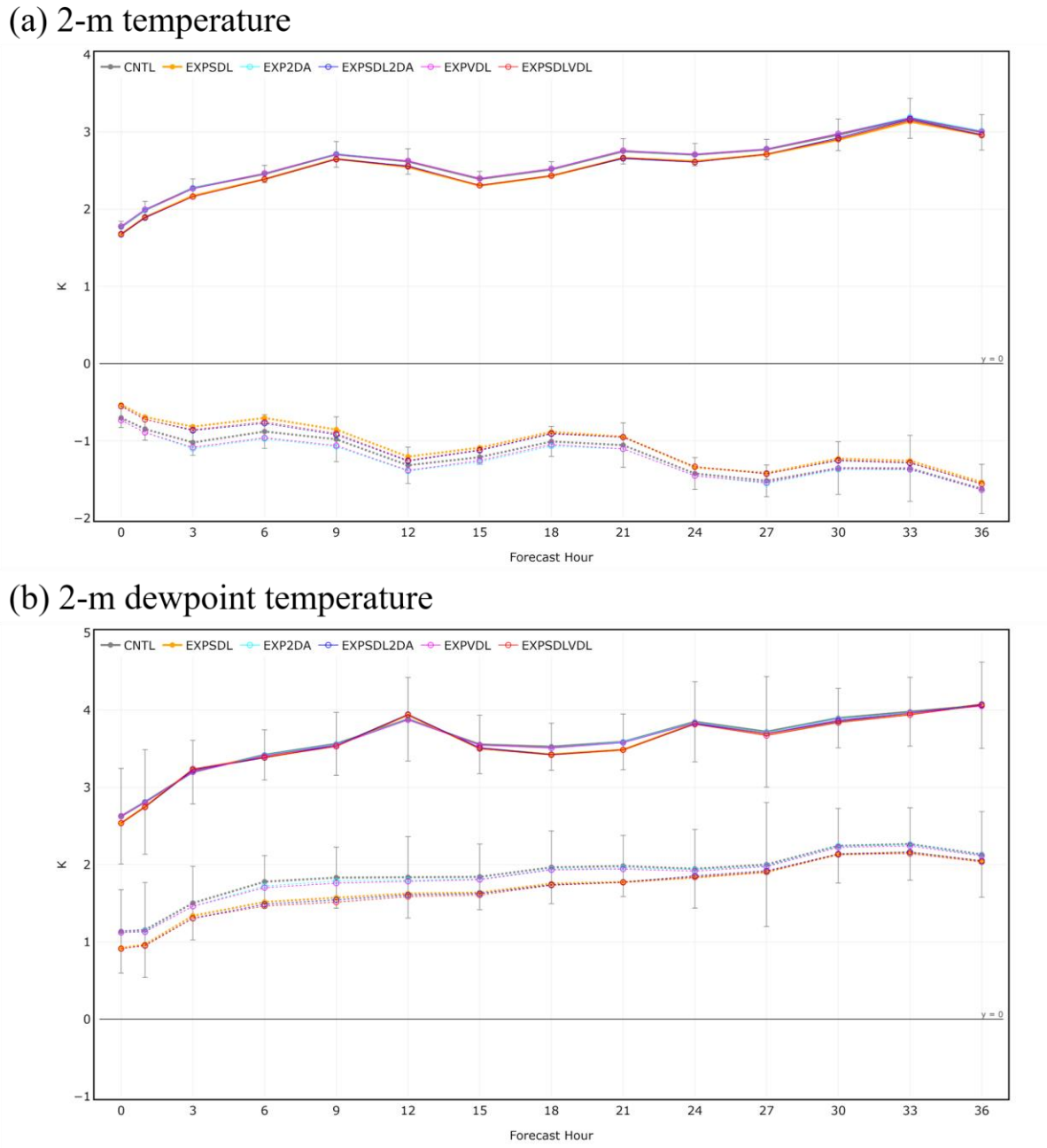


Fig. 8. Forecast RMSE (solid lines) and bias (dotted lines) verified against (a) temperature (K) and (b) dew point temperature (K) observations at 2-m AGL in each cycling experiment for May 11–19, 2021 (gray: CNTL; orange: EXPSDL; cyan: EXP2DA; blue: EXPSDL2DA; magenta: EXPVDL; red: EXPSDLVDL). The error bars show 95% confidence in CNTL.

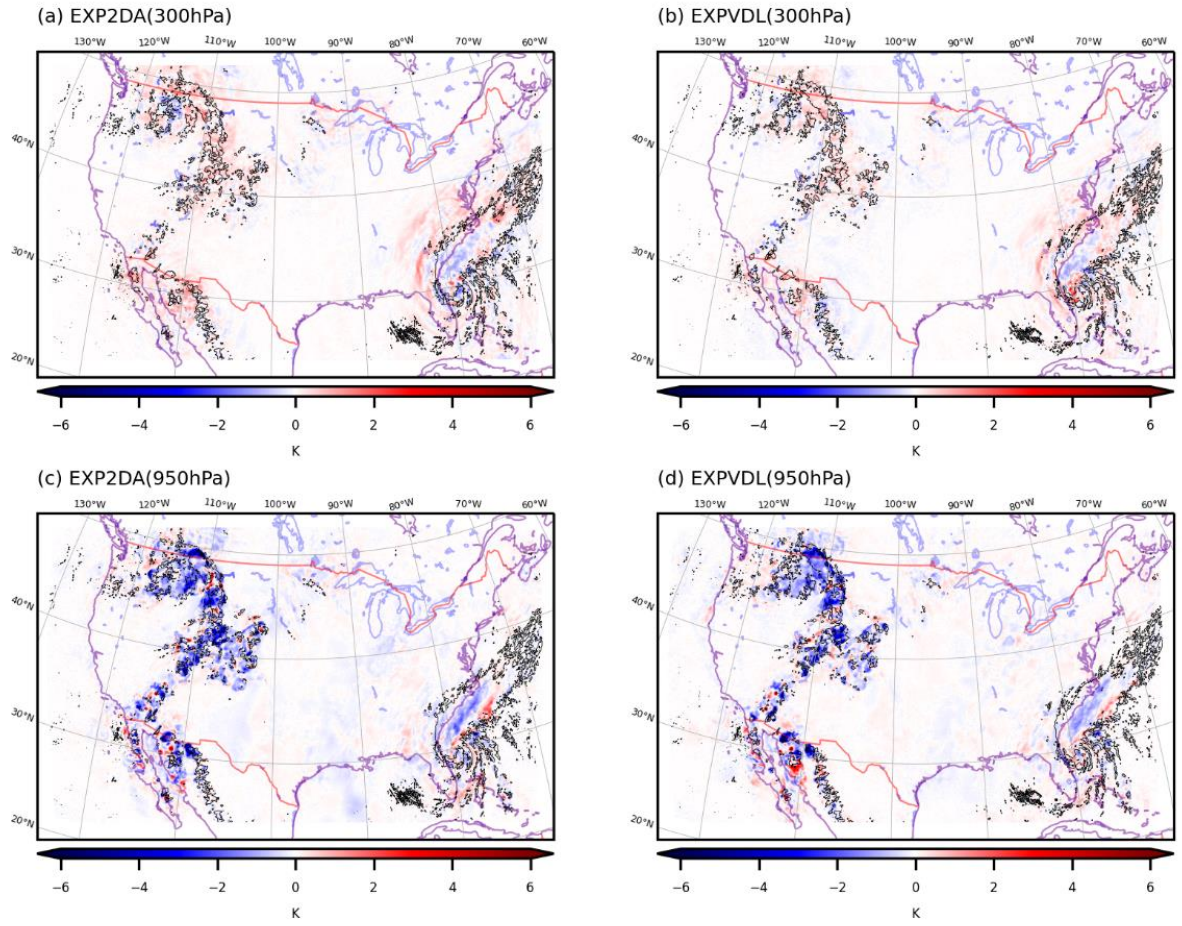


Fig. 9. Difference of 1-hour temperature forecasts in (a,b) 300 hPa and (c,d) 950 hPa at 00UTC, September 30, 2022 (a,c; EXP2DA-CNTL; b,d: EXPVDL-CNTL). Black contours are composited radar reflectivity forecasts (10 dBZ) in (a,c) EXP2DA and (b,d) EXPVDL.

(a) reflectivity 3-hour forecast

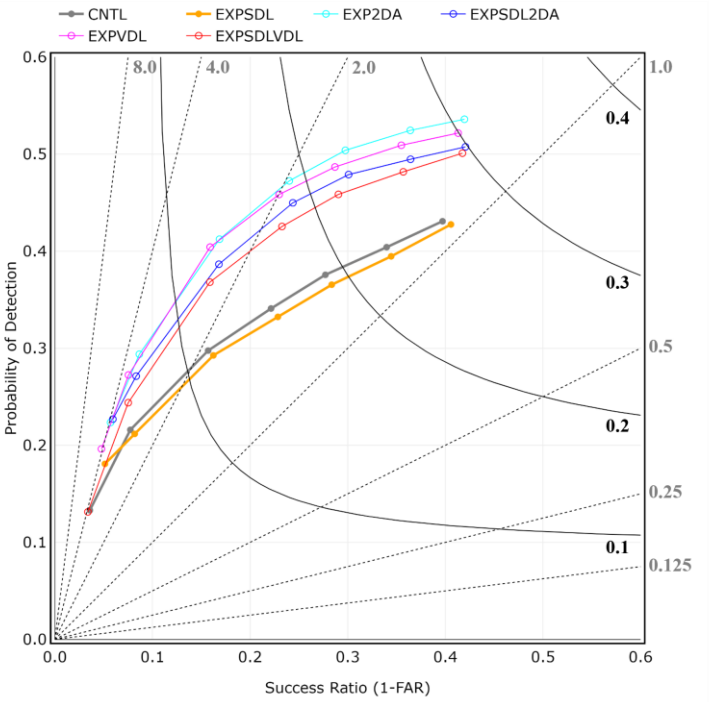


(b) reflectivity 12-hour forecast

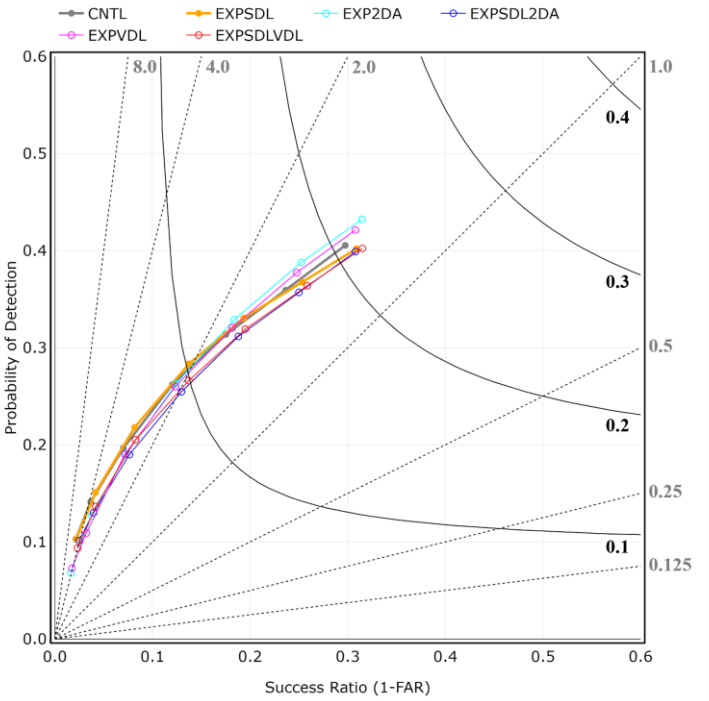


Fig. 10. Performance diagram of (a) 3-hour and (b) 12-hour radar reflectivity forecasts in each cycling experiment for May 11–19, 2021 (gray: CNTL; orange: EXPSDL; cyan: EXP2DA; blue: EXPSDL2DA; magenta: EXPVDL; red: EXPSDLVDL). Horizontal and vertical axes are SR and POD, respectively, verified against the MRMS composite reflectivity (thresholds: 15, 20, 25, 30, 35, 40, and 45 dBZ from higher SR and POD to lower). Bold numbers indicate CSI (gray) and bias (black).

411 *c. Impacts on the hurricane analysis and forecast*

412 In this section, the impacts of SDL and VDL shown in the previous section are discussed in
413 more detail based on the case of Hurricane Ian in September 2022. The cold bias of low-level
414 temperature seen in the period for May 11–19, 2021 was similarly decreased by SDL also in
415 the period for September 29–30, 2022 (not shown).

416 Figure 11 depicts the analysis increments of surface pressure in each experiment at 16 UTC,
417 September 29. In the experiments with SDL (Figs. 11b, d, and f), the analysis increment was
418 horizontally smoother than those without SDL (Figs. 11a, c, and e) because the larger
419 localization radius was applied for the larger-scale (smoothed) ensemble covariances in SDL.
420 As a result, SDL reduced the horizontally-averaged first guess departure more than the
421 experiments without SDL, which is why the bias of temperature and humidity was smaller in
422 the experiments with SDL for the May cycling period of experiments (Figs. 6–8).

423 The relative smoothness of the analysis increment is dependent on the power spectra of the
424 ensemble perturbations. For example, SDL also made the analysis increment of lowest-level
425 temperature smoother horizontally (not shown). However, it was not as smooth as surface
426 pressure because the power spectrum of large wavelength of lowest-level temperature was not
427 larger relatively than that of surface pressure. Figure 12 shows the power spectra of one-
428 member's ensemble perturbations of surface pressure and temperature used for ensemble-based
429 BEC in the EnVar analysis at 16 UTC, September 29, which indicates the contribution ratio of

power spectrum of larger wavelength to the whole was larger in surface pressure (Fig. 12a) than that in lowest-level temperature (Fig. 12b). Note that the power spectrum density ratio of ensemble perturbations separated by SDL (Fig. 2) did not depend on variables.

The smoother analysis increment caused by SDL does not necessarily decrease RMSE of the short-term forecast because the resulting analysis is not as close to the assimilated observations in the finer scale. However, it may be beneficial for the long-term forecast due to the smaller dynamical imbalance of the analysis. In fact, the mean surface pressure tendencies of the forecasts from the analyses at 00 UTC, September 30 were smaller in the experiments with SDL (Fig. 13).

Figure 13 also shows that radar reflectivity DA enlarged the imbalance. This tendency was seen especially in the experiments with SCL (EXP2DA and EXPSDL2DA) because the smaller horizontal localization in the second pass of 3DEnVar limited the analysis increments of atmospheric variables only near assimilated observations (dashed gray line in Fig. 3b) and made them noisy (northeast coast of Florida in Figs. 11c and d). In the experiments with VDL (EXPVDL and EXPSDLVDL), the analysis increment was less noisy even with radar reflectivity DA than that in the experiments with SCL (Figs. 11e and f) because the localization function of atmospheric variables was smaller and wider (magenta line in Fig. 3b). As a result, VDL kept the imbalance smaller even while assimilating radar reflectivity and the imbalance reduction by SDL was clearer than the experiments with SCL.

449 The imbalance reduction by SDL and VDL also affected the track forecast of Hurricane Ian
450 (Figs. 14 and 15). In the experiments with radar reflectivity DA (Figs. 14c–f), the composite
451 reflectivity analyses were closer to the MRMS observation than that in CNTL near the center
452 of Ian. However, the analyses of SLP were less axisymmetric, and the resulting track forecast
453 had larger cross-track error in the experiments with SCL (Figs. 14c and d) than those in the
454 other experiments (Fig. 15a). In the experiments with VDL (Figs. 14e and f), the cross-track
455 errors were as small as that in CNTL, and the composite reflectivity analyses were similar to
456 the experiments with SCL. On the other hand, the intensification forecast of Ian (Fig. 15c) was
457 a little overestimated in EXPVDL probably because the smaller imbalance was more suitable
458 for the hurricane intensification than EXP2DA. This overestimation was not seen in comparison
459 between EXPSDLVDL and EXPSDL2DA. The larger-scale, smoother analysis increment in
460 EXPSDLVDL might affect the intensification forecast. Note that these impacts were seen in the
461 specific forecast, and SDL and VDL do not necessarily improve the track and intensification
462 forecasts. More cases would need to be evaluated to assess the overall impact on tropical
463 cyclone forecasts.
464

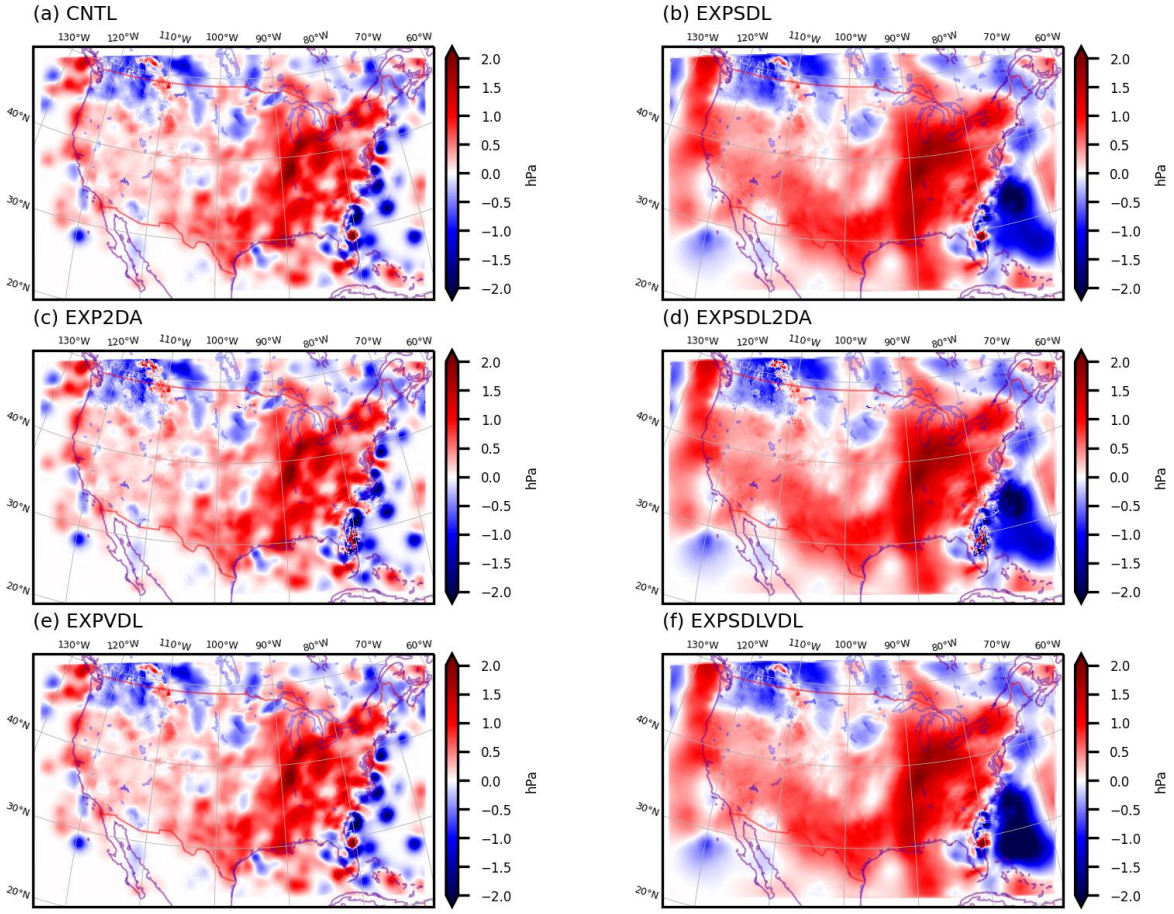


Fig. 11. Analysis increment of surface pressure (hPa) at 16UTC, September 29, 2022, in each experiment (a: CNTL; b: EXPSDL; c: EXP2DA; d: EXPSDL2DA; e: EXPVDL; f: EXPSDLVDL).

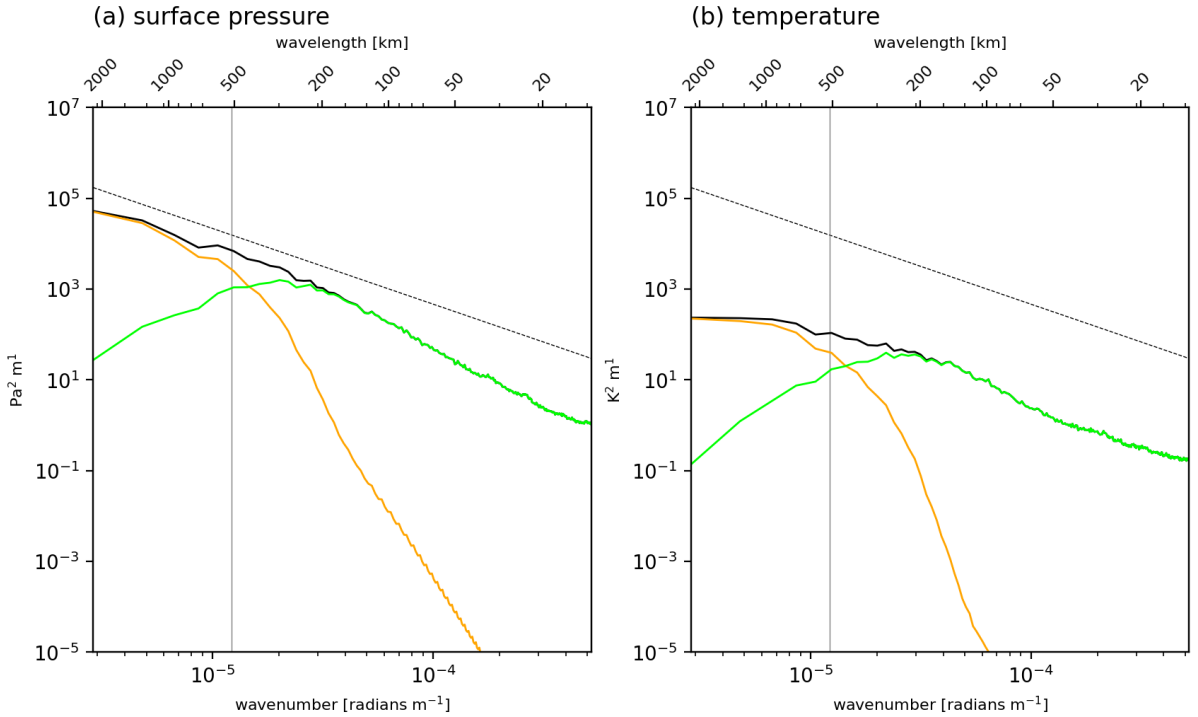


Fig. 12. The power spectra of (a) surface pressure ($Pa^2$ m) and (b) the lowest-level temperature ($K^2$ m), in the analysis at 16UTC on September 29, 2022, in EXPSDLVDL (black: original perturbation: orange: filtered perturbation by recursive filter; green: difference between original and filtered perturbations). Gray solid line indicates characteristic wavelength in scale separation (recursive filter $e^{-1/2}$-folding scale). Black dotted line indicates (wavenumber)$^{-5/3}$.

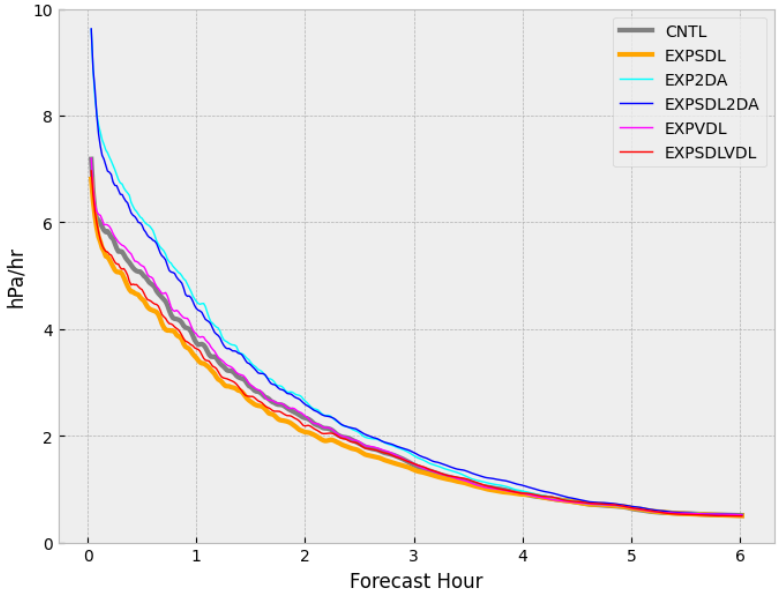


Fig. 13. Mean absolute pressure tendency (hPa $hr^{-1}$) of the first 6-hour forecasts from the analysis at 00 UTC, September 30, 2022 in each experiment (gray: CNTL; orange: EXPSDL; cyan: EXP2DA; blue: EXPSDL2DA; magenta: EXPVDL; red: EXPSDLVDL).

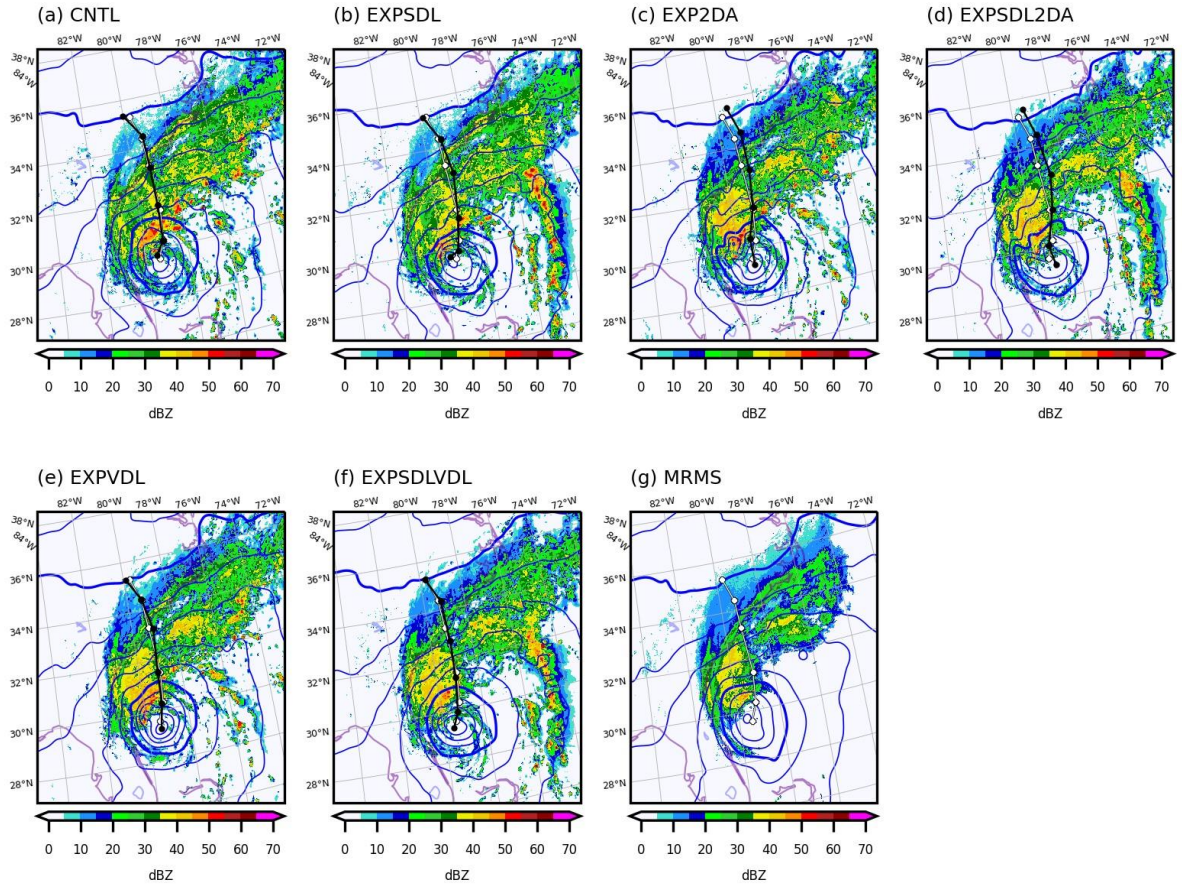


Fig. 14. Composited radar reflectivity (color, dBZ) and SLP (blue contours, every 4 hPa) analyses at 00UTC, September 30, 2022, and Hurricane Ian track forecasts (black lines) in each experiment (a: CNTL; b: EXPSDL; c: EXP2DA; d: EXPSDL2DA; e: EXPVDL; f: EXPSDLVDL) and (g) MRMS observations and HRRR SLP analysis. White lines are Ian's best track.

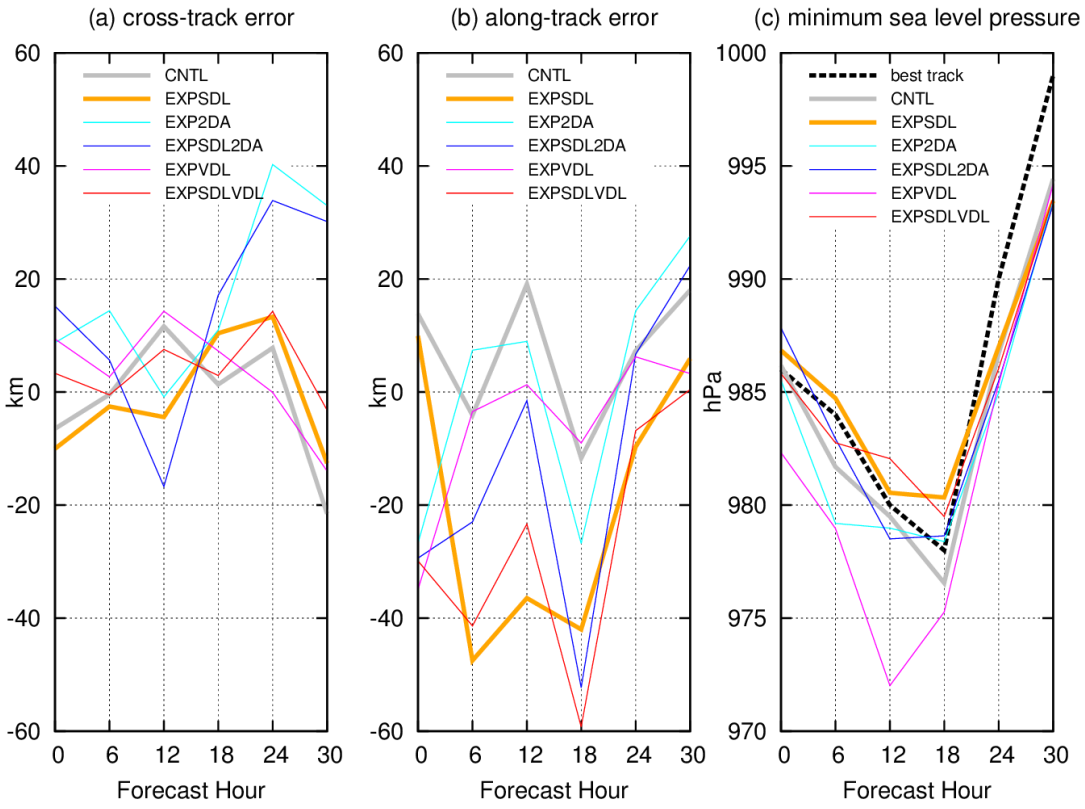


Fig. 15. (a) Cross-track error (positive: right of track) and (b) along-track error (positive: faster) verified against the best track (km) and (c) minimum sea level pressure (hPa) of Hurricane Ian forecasts initialized at 00UTC, September 30, 2022, in each experiment (gray: CNTL; orange: EXPSDL; cyan: EXP2DA; blue: EXPSDL2DA; magenta: EXPVDL; red: EXPSDLVDL). Black dotted line in (c) indicates the best track.

# 5. Conclusions

In this study, both scale- and variable-dependent localization (SDL and VDL) were implemented in a prototype RRFS. Through sensitivity tests we have shown several advantages of adopting SDL and VDL techniques for convective-scale DA based upon a week-long cycling test and a brief case study with Hurricane Ian.

The advantage of SDL is that the localization radius can be larger while keeping the effect of the sampling error small. It made the analysis increments smoother and was effective in improving the bias of the forecast of low-level temperature and relative humidity (Figs. 6–8) and at decreasing the dynamical imbalance of the analysis (Fig. 13). Although the smoother analysis increment does not necessarily decrease the RMSE of the short-term forecast, it may improve the long-term forecast. In particular, low-level temperature and precipitation were improved for 12-hour forecasts (Figs. 6–8).

On the other hand, the main advantage of VDL is to make the simultaneous conventional and radar reflectivity DA possible. In the conventional localization, the localization radii for all variables including hydrometeors cannot be optimized simultaneously. However, SCL generated a large imbalance due to too small localization radius for atmospheric variables in radar reflectivity DA (Fig. 13). In assimilating radar reflectivity by VDL, the imbalance became smaller than SCL (Fig. 13) because of the larger localization radius and the smaller analysis increment of atmospheric variables (Fig. 3b).

In both SDL and VDL, the imbalance reduction is important in considering implementation of them in the operational DA system. These methods are beneficial especially in the following situations: (i) the ensemble size is limited, (ii) the imbalance of the analysis largely affects the targeted forecast, and (iii) dense hydrometeor observations are assimilated simultaneously with the other sparse atmospheric observations. In operational regional DA systems, these limitations generally should be considered to assimilate many observations in a tight time limit.

SDL and VDL increase the memory usage and the computation time for the localization. However, the computational cost in VDL is smaller than that in SCL since the number of times of inputting files required to run EnVar (once) is less than that required in SCL (twice). In this study, the total computation time for EnVar was comparable between CNTL and EXPSDLVDL.

Since the weight of each scale in SDL is automatically determined depending on the power spectra of the variables, the sensitivity of the localization radius to the forecast is less than the case without SDL (not shown). However, tuning localization radii are still required even with SDL, and the optimal radii depend on variables, vertical levels, seasons, and so on. Adapting different localization radii separately for these components with techniques such as VDL may optimize the localization radii more strictly. However, it makes tuning them more complicated. To prevent manual tuning, new techniques such as the adaptive localization (e.g., Menetrier and Auligne 2015) should be developed also for SDL and VDL.

## Acknowledgments

The authors thank Xiaoyan Zhang for executing the statistical verification, RRFS developers in the NOAA Global Systems Laboratory for discussions on SDL and VDL testing, and Catherine Thomas and Matthew Pyle for their thoughtful reviews on an earlier version of this manuscript. We used one of the NOAA Research and Development High Performance Computing Systems (RDHPCS), ORION, located at Mississippi State University for conducting the experiments in this study.

## Data Availability Statement

Observation data used in this study are openly available at the NOAA Rapid Refresh (RAP) data registry of open data on AWS (https://registry.opendata.aws/noaa-rap/). The DA and forecast system, including the GSI and FV3LAM, used in this study can be obtained from https://github.com/shoyokota/ufs-srweather-app/commits/feature/RRFS_dev1_SDL_VDL.

# APPENDIX A

# Characteristic wavelength in scale separation with the recursive filter in SDL

The recursive filter $\mathbf{F}_{s,v}$ used for scale separation in Eq. (8) is working as a low-pass filter and the resulting power spectra of ensemble perturbations are quasi-Gaussian in wave space. This characteristic of scale separation is explained as follows.

Since the recursive filter is regarded as a quasi-Gaussian filter (Purser et al. 2003), the filtering kernel of $\mathbf{F}_{s,v}$ in the $x$-direction is approximated as Gaussian

$$F_\sigma(x) = \frac{1}{\sqrt{2\pi}\sigma} e^{-\frac{x^2}{2\sigma^2}}, \tag{A1}$$

where $\sigma$ is the $e^{-1/2}$-folding length of the recursive filter and $\int_{-\infty}^{\infty} F_\sigma(x)dx = 1$. Using this Eq. (A1), Fourier response of this $F_\sigma(x)$ is obtained as

$$G_\sigma(k) \equiv \int_{-\infty}^{\infty} F_\sigma(x) e^{-ikx} dx = e^{-\frac{k^2\sigma^2}{2}} \int_{-\infty}^{\infty} \frac{1}{\sqrt{2\pi}\sigma} e^{-\frac{(x+ik\sigma^2)^2}{2\sigma^2}} dx = e^{-\frac{k^2\sigma^2}{2}}. \tag{A2}$$

Eq. (A2) indicates that $G_\sigma(k)$ is also Gaussian in wave space and its characteristic wavenumber $k_c$ defined by $G_\sigma(k_c) \equiv e^{-1/2}$ is $k_c = 1/\sigma$. As a result, the characteristic wavelength of $G_\sigma(k)$ is $\lambda_c \equiv 2\pi/k_c = 2\pi\sigma$. Since the power spectrum density ratio of filtered ensemble perturbations (e.g., Fig. 2) is proportional to $G_\sigma(k)^2$, the ratio is about $e^{-1}$ in wavenumber of $\lambda_c = 2\pi\sigma$.

# APPENDIX B

# Localization of cross-variable covariance in VDL

In EXPVDL and EXPSDLVDL, the parameter making the cross-variable correlation smaller was applied to mitigate overestimation of analysis increments. This overestimation is caused by the horizontally-integrated localization function in VDL, which is larger than that applied for radar reflectivity in general. Details are explained as follows.

When the filtering kernels of $\mathbf{L}_{s,v}$ and $\mathbf{L}_{s,v}^{1/2}$ in $x$-direction are written as $L_\sigma(x)$ and $C_\sigma(x)$, respectively, their relationship should be written as:

$$L_\sigma(x) = \int_{-\infty}^{\infty} C_\sigma(x - x')C_\sigma(x')dx' = e^{-\frac{x^2}{2\sigma^2}}. \tag{B1}$$

Note that the normalization factor is different between $L_\sigma(x)$ in Eq. (B1) and $F_\sigma(x)$ in Eq. (A1) because the peak value of $\mathbf{L}_{s,v}$ should be one. From this Eq. (B1), $C_\sigma(x)$ is obtained as:

$$C_\sigma(x) = \left(\frac{2}{\pi\sigma^2}\right)^{1/4} e^{-\frac{x^2}{\sigma^2}}. \tag{B2}$$

Using this Eq. (B2), the localization applied for cross-variable covariances in VDL is based on the following kernel:

$$L_{\sigma_1,\sigma_2}(x) = \int_{-\infty}^{\infty} C_{\sigma_1}(x - x')C_{\sigma_2}(x')dx' = \sqrt{\frac{2\sigma_1\sigma_2}{\sigma_1^2 + \sigma_2^2}}\, e^{-\frac{x^2}{\sigma_1^2+\sigma_2^2}}, \tag{B3}$$

where $\sigma_1 \gg \sigma_2$. According to Eq. (B3), the peak value of $L_{\sigma_1,\sigma_2}(x)$ is less than one, and the ratio of horizontally-integrated $L_{\sigma_1,\sigma_2}(x)L_{\sigma_1,\sigma_2}(y)$ and $L_{\sigma_2}(x)L_{\sigma_2}(y)$ is calculated as:

$$\frac{\int_{-\infty}^{\infty} L_{\sigma_1,\sigma_2}(x)L_{\sigma_1,\sigma_2}(y)dxdy}{\int_{-\infty}^{\infty} L_{\sigma_2}(x)L_{\sigma_2}(y)dxdy} = \frac{\sigma_1}{\sigma_2} \gg 1. \tag{B4}$$

578 Eq. (B4) means that the total assimilation effect of the variables localized by $L_{\sigma_1,\sigma_2}(x)L_{\sigma_1,\sigma_2}(y)$
579 in VDL is $\sigma_1/\sigma_2$ times as large as that by $L_{\sigma_2}(x)L_{\sigma_2}(y)$ in the single-scale localization. The
580 larger assimilation effect does not necessarily make the analysis increment larger in case the
581 effects of multiple observations are canceled by each other. However, they are not canceled in
582 case the first guess departure of radar reflectivity has large bias. To mitigate this overestimation
583 of the analysis increment in this case, multiplying the factor ($\leq \sigma_2/\sigma_1$) to $L_{\sigma_1,\sigma_2}(x)L_{\sigma_1,\sigma_2}(y)$
584 is effective. The solid gray, dashed gray, and magenta lines in Fig. 3b indicates the distributions
585 of $L_{\sigma_1}(x)L_{\sigma_1}(y)$, $L_{\sigma_2}(x)L_{\sigma_2}(y)$, and $(\sigma_2/\sigma_1)L_{\sigma_1,\sigma_2}(x)L_{\sigma_1,\sigma_2}(y)$, respectively, against $r =$
586 $\sqrt{x^2+y^2}$ in the case of $\sigma_2/\sigma_1 = 15/300 = 0.05$.
587

# REFERENCES


Angevine, W. M., Olson, J., Gristey, J. J., Glenn, I., Feingold, G., & Turner, D. D. (2020). Scale Awareness, Resolved Circulations, and Practical Limits in the MYNN-EDMF Boundary Layer and Shallow Cumulus Scheme. *Monthly Weather Review*, **148**(11), 4629–4639. https://doi.org/10.1175/mwr-d-20-0066.1

Beljaars, A. C. M., Brown, A. R., & Wood, N. (2004). A new parametrization of turbulent orographic form drag. *Quarterly Journal of the Royal Meteorological Society*, **130**(599), 1327–1347. https://doi.org/10.1256/qj.03.73

Benjamin, S. G., Devenyi, D., Weygandt, S. S., Brundage, K. J., Brown, J. M., Grell, G. A., Kim, D, Schwartz, B. E., Smirnova, T. G., Smith, T. L., & Manikin, G. S. (2004). An hourly assimilation–forecast cycle: The RUC. *Monthly Weather Review*, **132**(2), 495–518, https://doi.org/10.1175/1520-0493(2004)132<0495:AHACTR>2.0.CO;2

Benjamin, S. G., Weygandt, S. S., Brown, J. M., Hu, M., Alexander, C. R., Smirnova, T. G., Olson, J. B., James, E. P., Dowell, D. C., Grell, G. A., Lin, H., Peckham, S. E., Smith, T. L., Moninger, W. R., Kenyon, J. S., & Manikin, G. S. (2016). A North American hourly assimilation and model forecast cycle: The Rapid Refresh. *Monthly Weather Review*, **144**(4), 1669–1694, https://doi.org/10.1175/MWR-D-15-0242.1

Benjamin, S. G., Smirnova, T. G., James, E. P., Lin, L.-F., Hu, M., Turner, D. D., & He, S. (2022). Land-snow data assimilation including a moderately coupled initialization

method applied to NWP. *Journal of Hydrometeorology*, **23**(6), 825–845. https://doi.org/10.1175/JHM-D-21-0198.1

Benjamin, S. G., James, E. P., Hu, M., Alexander, C. R., Ladwig, T. T., Brown, J. M., Weygandt, S. S., Turner, D. D., Minnis, P., Smith, W. L., & Heidinger, A. K. (2021). Stratiform Cloud-Hydrometeor Assimilation for HRRR and RAP Model Short-Range Weather Prediction. *Monthly Weather Review*, **149**(8), 2673–2694. https://doi.org/10.1175/MWR-D-20-0319.1

Black, T. L., & Coauthors (2021). A Limited Area Modeling Capability for the Finite-Volume Cubed-Sphere (FV3) Dynamical Core and Comparison With a Global Two-Way Nest. *Journal of Advances in Modeling Earth Systems*, **13**(6), e2021MS002483. https://doi.org/10.1029/2021MS002483

Bucci, L., Alaka, L., Hagen, A., Delgado, S., & Beven, J. (2023). Hurricane Ian (AL092022). *National Hurricane Center Tropical Cyclone Report*, 72pp, https://www.nhc.noaa.gov/data/tcr/AL092022_Ian.pdf

Buehner, M. (2012). Evaluation of a spatial/spectral covariance localization approach for atmospheric data assimilation. *Monthly Weather Review*, **140**(2), 617–636. https://doi.org/10.1175/MWR-D-10-05052.1

Buehner, M., & Shlyaeva, A. (2015). Scale-dependent background-error covariance localisation. *Tellus A*, **67**(1), 28027, https://doi.org/10.3402/tellusa.v67.28027

Carley, J. R., Pyle, M. E., Alexander, C. R., & Weygandt, S. (2023). On the Development of NOAA's Rapid Refresh Forecast System. *Working Group on Numerical Experimentation Research Activity in Earth System Modelling*, **53**, 5.07–5.08. https://wgne.net/bluebook/uploads/2023/docs/05_Carley_Jacob_RapidRefreshModel.pdf

Caron, J.-F., & Buehner, M. (2018). Scale-dependent background error covariance localization: Evaluation in a global deterministic weather forecasting system. *Monthly Weather Review*, **146**(5), 1367–1381. https://doi.org/10.1175/MWR-D-17-0369.1

Caron, J.-F., & Buehner, M. (2022). Implementation of scale-dependent background-error covariance localization in the Canadian global deterministic prediction system. *Weather and Forecasting*, **37**(9), 1567–1580. https://doi.org/10.1175/WAF-D-22-0055.1

Caron, J.-F., Michel, Y., Montmerle, T., & Arbogast, E. (2019). Improving background error covariances in a 3D ensemble-variational data assimilation system for regional NWP. *Monthly Weather Review*, **147**(1), 135–151. https://doi.org/10.1175/MWR-D-18-0248.1

Crum, T. D., & Alberty, R. L. (1993). The WSR-88D and the WSR-88D operational support facility. *Bulletin of the American Meteorological Society*, **74**(9), 1669–1688. https://doi.org/10.1175/1520-0477(1993)074<1669:TWATWO>2.0.CO;2

Dong, J. & Xue, M. (2013). Assimilation of radial velocity and reflectivity data from coastal WSR-88D radars using an ensemble Kalman filter for the analysis and forecast of

landfalling hurricane Ike (2008). *Quarterly Journal of the Royal Meteorological Society*, **139**(671), 467–487. https://doi.org/10.1002/qj.1970

Dowell, D. C., & Coauthors (2022). The High-Resolution Rapid Refresh (HRRR): An hourly updating convection-allowing forecast model. Part I: Motivation and system description. *Weather and Forecasting*, **37**(8), 1371–1395. https://doi.org/10.1175/WAF-D-21-0151.1

Evensen, G. (1994). Sequential data assimilation with a nonlinear quasi-geostrophic model using Monte Carlo methods to forecast error statistics. *Journal of Geophysical Research*, **99**(C5), 10143–10162. https://doi.org/10.1029/94JC00572

Gaspari, G., & Cohn, S. E. (1999). Construction of correlation functions in two and three dimensions. *Quarterly Journal of the Royal Meteorological Society*, **125**(554), 723–757. https://doi.org/10.1002/qj.49712555417

Greybush, S. J., Kalnay, E., Miyoshi, T., Ide, K., & Hunt, B. R. (2011). Balance and Ensemble Kalman Filter Localization Techniques. *Monthly Weather Review*, **139**(2), 511–522. https://doi.org/10.1175/2010MWR3328.1

Hamill, T. M., & Snyder, C. (2000). A hybrid ensemble Kalman filter-3D variational analysis scheme. *Monthly Weather Review*, **128**(8), 2905–2919. https://doi.org/10.1175/1520-0493(2000)128<2905:AHEKFV>2.0.CO;2

Hamill, T. M., Whitaker, J. S. & Snyder, C. (2001). Distance-dependent filtering of background error covariance estimates in an ensemble Kalman filter. *Monthly Weather*

*Review*, **129**(11), 2776–2790. https://doi.org/10.1175/1520-0493(2001)129<2776:DDFOBE>2.0.CO;2

Houtekamer, P. L., & Mitchell, H. L. (2001). A sequential ensemble Kalman filter for atmospheric data assimilation. *Monthly Weather Review*, **129**(1), 123–137. https://doi.org/10.1175/1520-0493(2001)129<0123:ASEKFF>2.0.CO;2

Huang, B., Wang, X., Kleist, D. T., & Lei, T. (2021). A simultaneous multiscale data assimilation using scale-dependent localization in GSI-based hybrid 4DEnVar for NCEP FV3-based GFS. *Monthly Weather Review*, **149**(2), 479–501. https://doi.org/10.1175/MWR-D-20-0166.1

Hunt, B. R., Kostelich, E. J., & Szunyogh, I. (2007). Efficient data assimilation for spatiotemporal chaos: A local ensemble transform Kalman filter. *Physica D*, **230**(1–2), 112–126. https://doi.org/10.1016/j.physd.2006.11.008

Iacono, M. J., Delamere, J. S., Mlawer, E. J., Shephard, M. W., Clough, S. A., & Collins, W. D. (2008). Radiative forcing by long-lived greenhouse gases: Calculations with the AER radiative transfer models. *Journal of Geophysical Research*, **113**(D13). D13103. https://doi.org/10.1029/2008JD009944

Janjic, Z. I. (2003). A nonhydrostatic model based on a new approach. *Meteorology and Atmospheric Physics*, **82**, 271–285. https://doi.org/10.1007/s00703-001-0587-6

Janjic, Z. I., & Gall, R. L. (2012). Scientific documentation of the NCEP nonhydrostatic multiscale model on the B grid (NMMB). Part 1: Dynamics (No. NCAR/TN-489+STR). University Corporation for Atmospheric Research, 75 pp. https://doi.org/10.5065/D6WH2MZX

Johnson, A. & Wang, X. (2017). Design and implementation of a GSI-based convection-allowing ensemble data assimilation and forecast system for the PECAN field experiment. Part I: optimal configurations for nocturnal convection prediction using retrospective cases. *Weather and Forecasting*, **32**(1), 289–315. https://doi.org/10.1175/WAF-D-16-0102.1

Lei, L., Whitaker, J. S., & Bishop, C. (2018). Improving assimilation of radiance observations by implementing model space localization in an ensemble Kalman filter. *Journal of Advances in Modeling Earth Systems*, **10**(12), 3221–3232. https://doi.org/10.1029/2018MS001468

Lin, S.-J. (2004). A "vertically lagrangian" finite-volume dynamical core for global models. *Monthly Weather Review*, **132**(10), 2293–2307. https://doi.org/10.1175/1520-0493(2004)132<2293:AVLFDC>2.0.CO;2

Liu, S., DiMego, G., Guan, S., Kumar, V. K., Keyser, D., Xu, Q., Nai, K., Zhang, P., Liu, L., Zhang, J., Howard, L., & Ator, J. (2016). WSR-88D Radar Data Processing at NCEP. *Weather and Forecasting*, **31**(6), 2047–2055. https://doi.org/10.1175/WAF-D-16-0003.1

Lorenc, A. C. (2003). The potential of the ensemble Kalman filter for NWP: a comparison with 4D-Var. *Quarterly Journal of the Royal Meteorological Society*, **129**(595), 3183–3203. https://doi.org/10.1256/qj.02.132

Menetrier, B., & Auligne, T. (2015): Optimized localization and hybridization to filter ensemble-based covariances. *Monthly Weather Review*, **143**(10), 3931–3947. https://doi.org/10.1175/MWR-D-15-0057.1

Michel, Y., Auligne, T., & Montmerle, T. (2011). Heterogeneous convective-scale background error covariances with the inclusion of hydrometeor variables. *Monthly Weather Review*, **139**(9), 2994–3015. https://doi.org/10.1175/2011MWR3632.1

Miyoshi, T., & Kondo, K. (2013). A multi-scale localization approach to an ensemble Kalman filter. *SOLA*, **9**, 170–173. https://doi.org/10.2151/sola.2013-038

Mlawer, E. J., Taubman, S. J., Brown, P. D., Iacono, M. J., & Clough, S. A. (1997). Radiative transfer for inhomogeneous atmospheres: RRTM, a validated correlated-k model for the longwave. *Journal of Geophysical Research*, **102**(D14), 16663–16682. https://doi.org/10.1029/97JD00237

Nakanishi, M., & Niino, H. (2009). Development of an improved turbulence closure model for the atmospheric boundary layer. *Journal of the Meteorological Society of Japan*, **87**(5), 895–912. http://doi.org/10.2151/jmsj.87.895

NCEI (2023). NOAA Storm Events Database. Accessed July 2023, https://www.ncdc.noaa.gov/stormevents/

Olson, J. B., Kenyon, J. S., Angevine, W. A., Brown, J. M., Pagowski, M., & Suselj, K. (2019). A Description of the MYNN-EDMF Scheme and the Coupling to Other Components in WRF–ARW. *NOAA Technical Memorandum OAR GSD*, **61**. https://doi.org/10.25923/n9wm-be49

Olson, J. B., Smirnova, T., Kenyon, J. S., Turner, D. D., Brown, J. M., Zheng, W., & Green, B. W. (2021). A Description of the MYNN Surface-Layer Scheme. *NOAA Technical Memorandum OAR GSL*, **67**. https://doi.org/10.25923/f6a8-bc75

Perianez, A., Reich, H., & Potthast, R. (2014). Optimal localization for ensemble Kalman filter systems. *Journal of the Meteorological Society of Japan*, **92**(6), 585–597. https://doi.org/10.2151/jmsj.2014-605

Purser, R. J., Wu, W. S., Parrish, D. F., & Roberts, N. M. (2003). Numerical aspects of the application of recursive filters to variational statistical analysis. Part I: Spatially homogeneous and isotropic Gaussian covariances. *Monthly Weather Review*, **131**(8), 1524–1535. https://doi.org/10.1175//1520-0493(2003)131<1524:NAOTAO>2.0.CO;2

Putman, W. M., & Lin, S.-J. (2007). Finite-volume transport on various cubed-sphere grids. *Journal of Computational Physics*, **227**(1), 55–78. https://doi.org/10.1016/j.jcp.2007.07.022

737 Roberts, B., Jirak, I. L., Clark, A. J., Weiss, S. J., & Kain, J. S. (2019). Postprocessing and
738 visualization techniques for convection-allowing ensembles. *Bulletin of the American*
739 *Meteorological Society*, **100**(7), 1245–1258. https://doi.org/10.1175/BAMS-D-18-0041.1
740 Roberts, B., Gallo, B. T., Jirak, I. L., Clark, A. J., Dowell, D. C., Wang, X., & Wang, Y.
741 (2020). What does a convection-allowing ensemble of opportunity buy us in forecasting
742 thunderstorms? *Weather and Forecasting*, **35**(6), 2293–2316.
743 https://doi.org/10.1175/WAF-D-20-0069.1
744 Roebber, P. J. (2009). Visualizing Multiple Measures of Forecast Quality. *Weather and*
745 *Forecasting*, **24**(2), 601–608. https://doi.org/10.1175/2008WAF2222159.1
746 Smirnova, T. G., Brown, J. M., & Benjamin, S. G. (1997). Performance of different soil
747 model configurations in simulating ground surface temperature and surface fluxes.
748 *Monthly Weather Review*, **125**(8), 1870–1884. https://doi.org/10.1175/1520-
749 0493(1997)125<1870:PODSMC>2.0.CO;2
750 Smirnova, T. G., Brown, J. M., Benjamin, S. G. & Kim, D. (2000). Parameterization of cold-
751 season processes in the MAPS land-surface scheme. *Journal of Geophysical Research*,
752 **105**(D3), 4077–4086. https://doi.org/10.1029/1999JD901047
753 Smirnova, T. G., Brown, J. M., Benjamin, S. G., & Kenyon, J. S. (2016). Modifications to the
754 Rapid Update Cycle land surface model (RUC LSM) available in the weather Research

and forecasting model. *Monthly Weather Review*, **144**(5), 1851–1865. https://doi.org/10.1175/MWR-D-15-0198.1

Smith, T. M., & Coauthors (2016). Multi-Radar Multi-Sensor (MRMS) severe weather and aviation products: Initial operating capabilities. *Bulletin of the American Meteorological Society*, **97**(9), 1617–1630. https://doi.org/10.1175/BAMS-D-14-00173.1

Thompson, G., & Eidhammer, T. (2014). A Study of Aerosol Impacts on Clouds and Precipitation Development in a Large Winter Cyclone. *Journal of the Atmospheric Sciences*, **71**(10), 3636–3658. https://doi.org/10.1175/jas-d-13-0305.1

Tsiringakis, A., Steeneveld, G. J., & Holtslag, A. A. M. (2017). Small-scale orographic gravity wave drag in stable boundary layers and its impact on synoptic systems and near-surface meteorology. *Quarterly Journal of the Royal Meteorological Society*, **143**(704), 1504–1516. https://doi.org/10.1002/qj.3021

Wang, X., Parrish, D., Kleist, D., & Whitaker, J. (2013). GSI 3DVar-based ensemble–variational hybrid data assimilation for NCEP global forecast system: Single-resolution experiments. *Monthly Weather Review*, **141**(11), 4098–4117. https://doi.org/10.1175/MWR-D-12-00141.1

Wang, Y., & Wang, X. (2017). Direct assimilation of radar reflectivity without tangent linear and adjoint of the nonlinear observation operator in the GSI-based EnVar system: Methodology and experiment with the 8 May 2003 Oklahoma City tornadic supercell.

774 *Monthly Weather Review*, **145**(4), 1447–1471. https://doi.org/10.1175/MWR-D-16-
775 0231.1
776 Wang, Y., & Wang, X. (2023a). Simultaneous multiscale data assimilation using scale- and
777 variable-dependent localization in EnVar for convection allowing analyses and forecasts:
778 Methodology and experiments for a tornadic supercell. *Journal of Advances in Modeling*
779 *Earth Systems*, **15**(5), e2022MS003430. https://doi.org/10.1029/2022MS003430
780 Wang, Y., & Wang, X. (2023b). Improving CONUS convective-scale forecasting with
781 simultaneous multiscale data assimilation: A squall line case study. *Journal of*
782 *Geographical Research: Atmospheres*, submitted.
783 Wang, X., Chipilski, H. G., Bishop, C. H., Satterfield, E., Baker, N., & Whitaker, J. S. (2021).
784 A multiscale local gain form ensemble transform Kalman filter (MLGETKF). *Monthly*
785 *Weather Review*, **149**(3), 605–622. https://doi.org/10.1175/MWR-D-20-0290.1
786 Whitaker, J. S., & Hamill, T. M. (2002). Ensemble data assimilation without perturbed
787 observations. *Monthly Weather Review*, **130**(7), 1913–1924.
788 https://doi.org/10.1175/1520-0493(2002)130<1913:EDAWPO>2.0.CO;2
789 Whitaker, J. S., & Hamill, T. M. (2012). Evaluating methods to account for system errors in
790 ensemble data assimilation. *Monthly Weather Review*, **140**(9), 3078–3089.
791 https://doi.org/10.1175/MWR-D-11-00276.1

Zhang, F., Weng, Y., Sippel, J. A., Meng, Z., & Bishop, C. H. (2009). Cloud-resolving hurricane initialization and prediction through assimilation of Doppler radar observations with an ensemble Kalman filter. *Monthly Weather Review*, **137**(7), 2105–2125. https://doi.org/10.1175/2009MWR2645.1